

An improved approach to Bayesian computer model calibration and prediction

Mengyang Gu and Long Wang

Department of Applied Mathematics and Statistics
Johns Hopkins University

Abstract

We consider the problem of calibrating inexact computer models using experimental data. To compensate for the misspecification of the computer model, a discrepancy function is usually included and modeled via a Gaussian stochastic process (GaSP), leading to better results of prediction. The calibrated computer model itself, however, sometimes fits the experimental data poorly, as the calibration parameters become unidentifiable. In this work, we propose the scaled Gaussian stochastic process (S-GaSP), a novel stochastic process for calibration and prediction. This new approach bridges the gap between two predominant methods, namely the L_2 calibration and GaSP calibration. A computationally feasible approach is introduced for this new model under the Bayesian paradigm. Compared with the GaSP calibration, the calibrated parameters are more interpretable in the S-GaSP calibration, which enables the calibrated computer model itself to predict well on the reality. Simulated and real examples are provided to illustrate the connections and differences between this new model and other previous approaches.

KEYWORDS: Discrepancy function; Inverse problem; Model misspecification; Scaled Gaussian stochastic process

1 Introduction

Computer models or simulators are increasingly used to reproduce the behavior of complex systems in physics, engineering and human processes. These models are essentially computer implementations of mathematical models aiming to generate outputs based on a collection of inputs, such as initial conditions or model parameters. The true values of some model parameters, however, are unknown or unobservable in experiments. One of the fundamental tasks in uncertainty quantification is adjusting those unknown parameters until the outputs of the model fit the observed data, which is often referred as calibration of the computer model.

Assume one obtains a set of field data from experiments at \mathbf{x}_i , denoted as $y^F(\mathbf{x}_i)$ for $i = 1, \dots, n$. The computer model outputs, defined as $f^M(\mathbf{x}, \boldsymbol{\theta})$, are evaluated at the variable input $\mathbf{x} \in \mathcal{X}$ and calibration parameter $\boldsymbol{\theta}$. For simplicity, \mathcal{X} is assumed to be a bounded rectangle in \mathbb{R}^{p_x} and $\boldsymbol{\theta} \in \mathbb{R}^{p_\theta}$. If the computer model has no bias to the reality, meaning that the field data is a noisy

realization of the computer model for some set of parameters, then calibration is to choose $\boldsymbol{\theta}$ that minimizes the distance between the field data and outputs of the computer model.

In practice, a perfect computer model to the reality is rarely the case. It is common to address the model misspecification by a discrepancy function, such that the reality can be represented as $y^R(\mathbf{x}) = f^M(\mathbf{x}, \boldsymbol{\theta}) + \delta(\mathbf{x})$, where $y^R(\cdot)$ and $\delta(\cdot)$ denote the reality and discrepancy function, respectively. It leads to the following statistical model for calibration (Kennedy and O’Hagan, 2001),

$$y^F(\mathbf{x}) = f^M(\mathbf{x}, \boldsymbol{\theta}) + \delta(\mathbf{x}) + \epsilon, \quad (1)$$

where ϵ is a zero-mean noise. This model is investigated in a vast amount of literature (Bayarri et al., 2007b; Qian and Wu, 2008; Higdon et al., 2008; Liu et al., 2009). Unfortunately, many following-up studies found that the use of (1) sometimes results in an identifiability problem of $\boldsymbol{\theta}$ (Arendt et al., 2012a,b; Tuo and Wu, 2016; Plumlee, 2016).

To some extent, this identifiability problem is inherently rooted in (1). Suppose that the field data is noise-free and the discrepancy function is defined as $\delta_{\boldsymbol{\theta}}(\mathbf{x}) = y^F(\mathbf{x}) - f^M(\mathbf{x}, \boldsymbol{\theta})$, then the reality can always be modeled perfectly well regardless of the choice of $\boldsymbol{\theta}$. Much effort has been made to eliminate the identifiability issue recently. We briefly review two popular approaches in Section 1.1 and Section 1.2.

1.1 L_2 calibration

In Tuo and Wu (2016) and Tuo et al. (2015), the “optimal” calibration parameter $\boldsymbol{\theta}$ is defined as the one that minimizes the L_2 norm of the discrepancy function (henceforth the L_2 calibration), i.e.,

$$\boldsymbol{\theta}_{L_2} = \underset{\boldsymbol{\theta}}{\operatorname{argmin}} \|\delta_{\boldsymbol{\theta}}(\cdot)\|_{L_2(\mathcal{X})} = \underset{\boldsymbol{\theta}}{\operatorname{argmin}} \left\{ \int_{\mathbf{x} \in \mathcal{X}} [y^R(\mathbf{x}) - f^M(\mathbf{x}, \boldsymbol{\theta})]^2 d\mathbf{x} \right\}^{1/2}. \quad (2)$$

Note $y^R(\cdot)$ is not observable when the experimental data is noisy. A two-step approach is proposed in Tuo et al. (2015), where a Gaussian stochastic process is first utilized to estimate the reality $y^R(\cdot)$ and then estimator, $\hat{y}^R(\cdot)$, is plugged in (2) to obtain the L_2 calibration estimator. This approach is shown to converge to $\boldsymbol{\theta}_{L_2}$ in probability and achieves semi-parametric efficiency as the uniformly sampled inputs go to infinity. It is a very sensible approach, as the calibrated computer model explains as much variability in the reality as it can, and the calibration parameters are typically more interpretable scientifically.

A related method to L_2 calibration is the least squares (LS) estimator, which minimizes the squared error between the experimental data and computer model, i.e.,

$$\hat{\boldsymbol{\theta}}_{LS} = \underset{\boldsymbol{\theta}}{\operatorname{argmin}} \sum_{i=1}^n [y^F(\mathbf{x}_i) - f^M(\mathbf{x}_i, \boldsymbol{\theta})]^2. \quad (3)$$

It is shown in Tuo et al. (2015) and Wong et al. (2017) that $\hat{\boldsymbol{\theta}}_{LS}$ also converges to $\boldsymbol{\theta}_{L_2}$ in probability under some mild conditions, but it is generally less efficient than the L_2 calibration unless the computer model is perfect. When the sample size is relatively large, $\hat{\boldsymbol{\theta}}_{LS}$ is similar to the estimator of $\boldsymbol{\theta}$ in the two-step L_2 calibration.

The discrepancy function, however, is not modeled in the L_2 calibration. For instance, the LS estimator is equivalent to the maximum likelihood estimator (MLE) of $\boldsymbol{\theta}$ in (1) with zero-mean

independent Gaussian noise and no discrepancy. The lacking assumption of the discrepancy function is often undesired in practice, as modeling the discrepancy function along with the computer model provides a sampling model for the reality, which typically yields a good result of prediction. Besides, the L_2 calibration only provides a point estimator for $\boldsymbol{\theta}$ without taking account of the parameter uncertainty, and the single best model defined by the L_2 calibration is not always equivalent to the most desirable model (Brynjarsdóttir and O’Hagan, 2014).

1.2 GaSP calibration

In Kennedy and O’Hagan (2001), the discrepancy function is specified as a Gaussian stochastic process (GaSP) (henceforth the GaSP calibration). As modeling the discrepancy through a GaSP provides a flexible sampling model for the experimental data, the prediction of the unobserved field data, based on both the calibrated computer model and discrepancy function, is empirically better than using the calibrated computer model alone (Kennedy and O’Hagan, 2001). Despite this benefit, modeling the discrepancy function through a GaSP sometimes overwhelms the effects of the computer model when the residuals between the experimental data and computer model outputs are correlated, resulting in an identifiability issue of the calibration parameters.

Here we provide an example to illustrate the identifiability problem in the GaSP calibration when the data is correlated. Consider a simple example where the computer model contains only a mean parameter, i.e., $f^M(x, \theta) = \theta$, with the true parameter being $\theta^* = 0$. Assume one obtains $n = 200$ observations, denoted as $\mathbf{y}^F = (y^F(x_1), \dots, y^F(x_{200}))^T$, sampled from a zero mean multivariate normal distribution at $x_i = (i - 1)/199$ for $i = 1, \dots, 200$

$$\mathbf{y}^F \sim MN(\mathbf{0}, \sigma_\delta^2 \mathbf{R}), \quad (4)$$

with $\sigma_\delta^2 = 1$ and the (i, j) term of \mathbf{R} being $R_{i,j} = \exp[-(|x_i - x_j|/\gamma^\delta)^{1.9}]$ for some γ^δ . Only two values of the calibration parameter are considered: $\theta = 0$ and $\theta = 1$, indicating the true model and misspecified model, respectively. Assume there is no further prior information and all the information to infer θ comes from the likelihood function.

Under different γ^δ , the natural logarithm of the likelihood (log-likelihood) function of these two models from 100 simulations is graphed in Figure 1. When $\gamma^\delta = 1$ and $\gamma^\delta = 1/10$, the log-likelihood of a true model is only 0.93 and 3.50 larger than the misspecified model on average, respectively. When the data is moderately correlated, the truth is barely identifiable, even if the data is sampled from a GaSP. In contrast, when the samples are independent, the expected difference of the log-likelihood between the two models is 100, meaning that the data is $\exp(100) \approx 2.69 \times 10^{43}$ more likely to be sampled from the true model than the misspecified model.

Typically, the independent sample is regarded as the perfect sample for inference. In this example, the expected difference of the log-likelihood between $\theta = 0$ and $\theta = 1$ is 1 when there are $n = 2$ independent samples. However, the average difference of the log-likelihood is only 0.93 between the true and misspecified models with $n = 200$ correlated observations sampled from the multivariate normal distribution in (4) with $\gamma^\delta = 1$. In reality, conditional on the outputs of computer model, many samples can still be very correlated, one real example of which is analyzed in Section 4.2.

Although the GaSP model provides a flexible sampling model of the reality, the likelihood function of the GaSP model is very flat on the space of θ when the observations are moderately

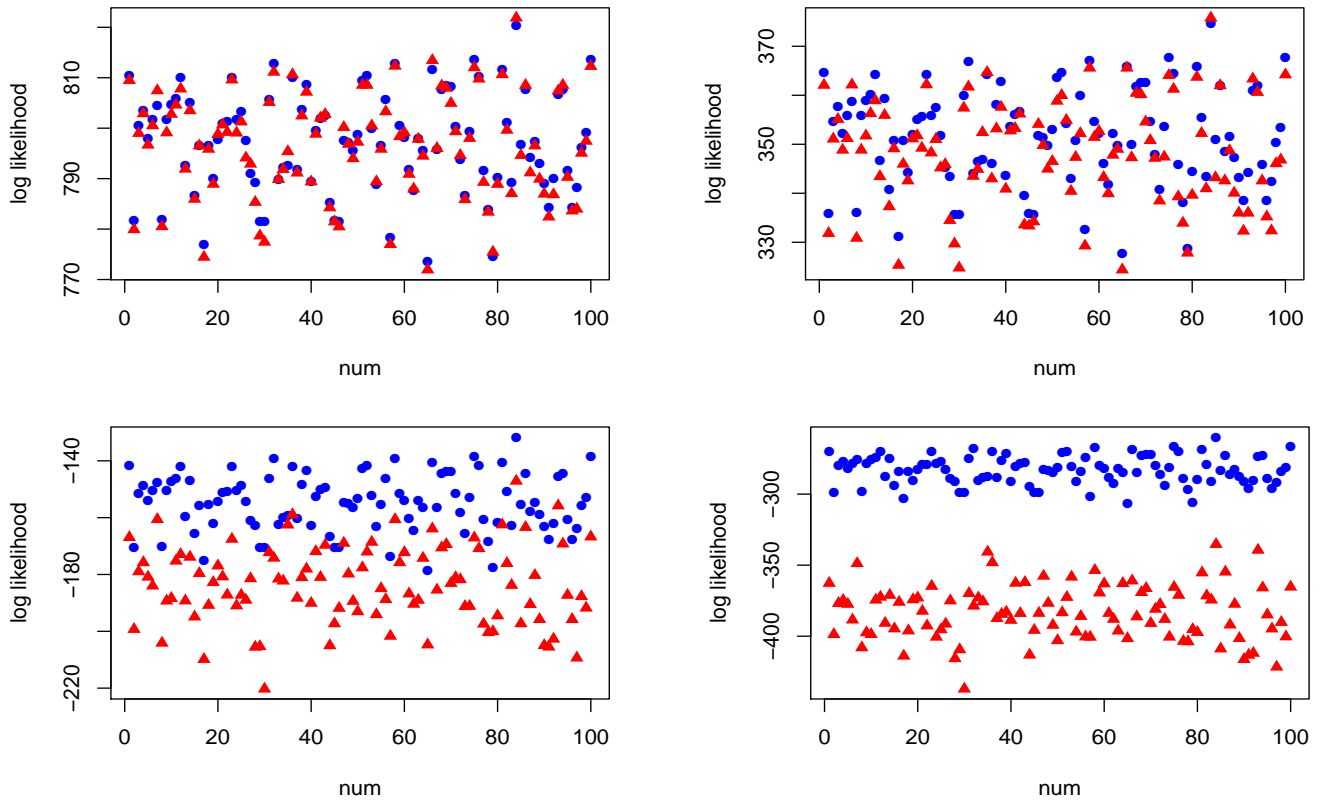


Figure 1: The log-likelihood function $\ell(\theta) := \log(p(\mathbf{y}^F | \theta))$ at different values of correlation. The observations are sampled from a zero mean multivariate normal distribution with the (i, j) entry of the covariance being $\exp[-(|x_i - x_j|/\gamma^\delta)^{1.9}]$. A hundred simulations are implemented in each case with $\gamma^\delta = \{1, 1/10, 1/100\}$ for the upper left, upper right and lower left panels respectively. The independent case is graphed in the lower right panel. The blue dots are $\ell(\theta = 0)$ (true model) and the red triangles are $\ell(\theta = 1)$ (misspecified model) in each simulation. The average difference of the log-likelihood between the true model and misspecified model is 0.93, 3.50, 28.91 and 100.41 for these four cases.

correlated. Consequently, the probability mass on those θ that has a smaller L_2 loss (the squared L_2 norm of the discrepancy function) is almost the same as those with a larger L_2 loss. The motivation of this study is to develop a stochastic process that is flexible enough for modeling the reality and simultaneously maintaining an adequate amount of probability mass on the small value of the L_2 loss between the computer and reality, especially for the case where observations are correlated.

1.3 Our contribution

In this paper, we introduce a new approach to reconcile the difference between the L_2 calibration and GaSP calibration. We develop a new stochastic process, called the scaled Gaussian stochastic process, and derive the closed-form likelihood of the new stochastic process. We also provide a computationally scalable approach that bypasses the usual Monte Carlo method to compute the likelihood. Our approach is introduced under the Bayesian framework, which contains both the point estimator and uncertainty quantification of the parameters through the posterior distributions. We evaluate the results of the calibration by the following two criteria.

- The proposed approach should predict the reality precisely by combining the calibrated computer model and discrepancy function.
- The calibrated computer model itself should also fit the observed data and predict the underlying true process well.

The first criterion requires an appropriate model of the discrepancy function when the computer model is misspecified, as the calibrated computer model and discrepancy could predict the reality better than using the calibrated computer model alone. The second criterion is from the L_2 calibration, as the computer model tends to be better calibrated and more interpretable, when it can predict the reality reasonably well. The interpretability of calibration parameters in the computer model depends on the specific background of the scientific problem, but one cannot say the calibration is successful if a calibrated computer model predicts the reality much worse than the same computer model with another set of parameters. Roughly put, a set of interpretable calibration parameters should allow the computer model to predict the reality relatively well even without the discrepancy function. The computer model, possibly along with some linear order discrepancy terms, is interpretable by scientists, while the added discrepancy function introduces some nonlinear effects that can be hard to be explained by scientific reasons. Therefore, we define the interpretability of a set of calibration parameters by measuring the predictive power of the calibrated computer model without a discrepancy function. We then demonstrate that the new approach performs better than the previous approaches based on these two criteria.

The remainder of the paper is organized as follows. We introduce the new calibration approach in Section 2 with a focus on the connection to the previous approaches. A computationally feasible way is also detailed under the Bayesian framework. We extend our approach to the case where the computer model is computationally expensive in Section 3. Real and simulated examples comparing our approach with the previous approaches are provided in Section 4. The concluding remarks and future directions are covered in Section 5.

2 Calibration and prediction by the scaled Gaussian stochastic process

The object of this section is to introduce an improved approach that overcomes the shortcomings in the L_2 calibration approach and GaSP calibration approach. The new model is proposed in Section 2.1. Section 2.2 introduces the reference choice of the measure of a key random variable, along with the connections between this new model and previous approaches. Section 2.3 provides a computational feasible way for the likelihood and predictive distribution. The prior specification and posterior computation are outlined in Section 2.4. The proofs of the lemmas are provided in the Appendix.

2.1 Scaled Gaussian stochastic process

We propose using the following model for calibration,

$$\begin{aligned} y^F(\mathbf{x}) &= f^M(\mathbf{x}, \boldsymbol{\theta}) + \mu^\delta(\mathbf{x}) + \delta_Z(\mathbf{x}) + \epsilon, \\ \delta_Z(\mathbf{x}) &= \left\{ \delta(\mathbf{x}) \mid \int_{\boldsymbol{\xi} \in \mathcal{X}} \delta(\boldsymbol{\xi})^2 d\boldsymbol{\xi} = Z \right\}, \\ \delta(\cdot) &\sim \text{GaSP}(0, \sigma_\delta^2 c^\delta(\cdot, \cdot)), \\ Z &\sim p_Z(\cdot), \epsilon \sim N(0, \sigma_0^2). \end{aligned} \tag{5}$$

We call $\delta_Z(\cdot)$ follows the scaled Gaussian stochastic process (S-GaSP). The innovation of the above model comes from the random variable Z . Given $Z = z$, the new process $\delta_Z(\cdot)$ is a GaSP $\delta(\cdot)$ constrained at the space of $\int_{\boldsymbol{\xi} \in \mathcal{X}} \delta(\boldsymbol{\xi})^2 d\boldsymbol{\xi} = z$. To sample the discrepancy function $\delta_Z(\cdot)$, we first sample $Z = z$ from the scaling density $p_Z(\cdot)$ and then sample $\delta(\cdot)$ constrained at the space of $\int_{\boldsymbol{\xi} \in \mathcal{X}} \delta(\boldsymbol{\xi})^2 d\boldsymbol{\xi} = z$. We introduce a practical way to compute the likelihood and to sample from the S-GaSP in Section 2.3.

In (5), $\mu^\delta(\cdot)$ is a mean discrepancy, typically modeled by regression,

$$\mu^\delta(\mathbf{x}) = \mathbf{h}^\delta(\mathbf{x}) \boldsymbol{\beta}^\delta = \sum_{i=1}^{q_\delta} h_i^\delta(\mathbf{x}) \beta_i^\delta, \tag{6}$$

where $\mathbf{h}^\delta(\mathbf{x}) = (h_1^\delta(\mathbf{x}), h_2^\delta(\mathbf{x}), \dots, h_{q_\delta}^\delta(\mathbf{x}))$ is a known q_δ -dimensional vector of basis functions and $\boldsymbol{\beta}^\delta = (\beta_1^\delta, \beta_2^\delta, \dots, \beta_{q_\delta}^\delta)^T$ is an unknown q_δ -dimensional vector with each β_i^δ being the regression parameter of $h_i^\delta(\mathbf{x})$ for $i = 1, \dots, q_\delta$.

As the mean discrepancy only contains the intercept and linear order terms which are easy to interpret, we treat it as a part of the computer model. The mean discrepancy benefits the prediction when the computer model does not contain the intercept or does not properly explain the trend with regard to the variable inputs. However, $\mu^\delta(\cdot)$ should be zero when the intercept and trend are properly modeled in the computer model.

$\delta(\cdot)$ is a zero-mean GaSP, meaning that the density of any $\{\mathbf{x}_1, \dots, \mathbf{x}_n\}$ takes the form of a multivariate normal

$$(\delta(\mathbf{x}_1), \dots, \delta(\mathbf{x}_n))^T \mid \mathbf{R}^\delta \sim \text{MN}(\mathbf{0}, \sigma_\delta^2 \mathbf{R}^\delta), \tag{7}$$

where \mathbf{R}^δ is a correlation matrix such that its (i, j) entry is defined as $R_{i,j}^\delta = c^\delta(\mathbf{x}_i, \mathbf{x}_j)$.

For any inputs $\mathbf{x}_a, \mathbf{x}_b \in \mathcal{X}$, the correlation is typically assumed to have a product form

$$c^\delta(\mathbf{x}_a, \mathbf{x}_b) = \prod_{l=1}^{p_x} c_l^\delta(x_{al}, x_{bl}), \quad (8)$$

where each $c_l^\delta(\cdot, \cdot)$ is a one-dimensional correlation function for the l^{th} coordinate of the input space. Power exponential correlation and Matérn correlation are widely used in GaSP models. The power exponential correlation has the following form

$$c_l^\delta(d_l) = \exp \left\{ - \left(\frac{d_l}{\gamma_l^\delta} \right)^{\nu_l^\delta} \right\}, \quad (9)$$

where $d_l = |x_{al} - x_{bl}|$ is the distance of the l^{th} coordinate of the input vectors; ν_l^δ is a roughness parameter typically held fixed and γ_l^δ is an unknown range parameter to be estimated.

The Matérn correlation has recently gained more interest in constructing GaSP emulator (Gu and Berger, 2017). The Matérn correlation with the roughness parameter $\nu_l^\delta = (2k + 1)/2$ for $k \in \mathbb{N}$ has a closed form expression. For instance, when $\nu_l^\delta = 5/2$, the Matérn correlation function is as follows:

$$c_l^\delta(d_l) = \left(1 + \frac{\sqrt{5}d_l}{\gamma_l^\delta} + \frac{5d_l^2}{3(\gamma_l^\delta)^2} \right) \exp \left(-\frac{\sqrt{5}d_l}{\gamma_l^\delta} \right), \quad (10)$$

where γ_l^δ is an unknown range parameter. This covariance function was widely used in modeling spatially correlated data (Stein, 2012) and is becoming popular in the field of uncertainty quantification. It is also the default choice of several R packages for computer models (Roustant et al., 2012; Gu et al., 2016b). We use this correlation function herein for the demonstration purpose, and the method is applicable to any covariance function of interest.

Let $\boldsymbol{\gamma}^\delta = (\gamma_1^\delta, \dots, \gamma_{p_x}^\delta)^T$. The parameters in the S-GaSP model are denoted as Θ that contains $\{\boldsymbol{\theta}; \boldsymbol{\beta}^\delta; \boldsymbol{\gamma}^\delta; \sigma_\delta^2; \sigma_0^2\}$ and some possible parameters in the scaling density $p_Z(\cdot)$. Any marginal distribution of the S-GaSP at $\boldsymbol{\delta}_z = (\delta_z(\mathbf{x}_1), \dots, \delta_z(\mathbf{x}_n))^T$ for $\{\mathbf{x}_1, \dots, \mathbf{x}_n\}$ can be computed by marginalizing out Z as follows

$$\begin{aligned} p_{\delta_z}(\boldsymbol{\delta}_z | \Theta) &= \int_0^\infty p_\delta \left(\boldsymbol{\delta}_z \mid \int_{\boldsymbol{\xi} \in \mathcal{X}} \delta(\boldsymbol{\xi})^2 d\boldsymbol{\xi} = z, \Theta \right) p_Z(z | \Theta) dz \\ &= p_\delta(\boldsymbol{\delta}_z | \Theta) \int_0^\infty \frac{p_\delta \left(\int_{\boldsymbol{\xi} \in \mathcal{X}} \delta(\boldsymbol{\xi})^2 d\boldsymbol{\xi} = z \mid \boldsymbol{\delta}_z, \Theta \right)}{p_\delta \left(\int_{\boldsymbol{\xi} \in \mathcal{X}} \delta(\boldsymbol{\xi})^2 d\boldsymbol{\xi} = z \mid \Theta \right)} p_Z(z | \Theta) dz, \end{aligned} \quad (11)$$

where $p_\delta(\boldsymbol{\delta}_z | \Theta)$ is a multivariate normal density evaluated at $\boldsymbol{\delta}_z$ in (7).

By the properties of the multivariate normal distribution, it follows that

$$\delta(\cdot) \mid \boldsymbol{\delta}_z, \Theta \sim \text{GaSP}(\mu^{*\delta}(\cdot), \sigma_\delta^2 c^{*\delta}(\cdot, \cdot)),$$

where for any $\mathbf{x}^* \in \mathcal{X}$,

$$\mu^{*\delta}(\mathbf{x}^*) = \mathbf{r}^\delta(\mathbf{x}^*)^T (\mathbf{R}^\delta)^{-1} \boldsymbol{\delta}_z, \quad (12)$$

with $\mathbf{r}^\delta(\mathbf{x}^*) = (c^\delta(\mathbf{x}^*, \mathbf{x}_1), \dots, c^\delta(\mathbf{x}^*, \mathbf{x}_n))^T$ and for any $\mathbf{x}_a^*, \mathbf{x}_b^* \in \mathcal{X}$,

$$c^{*\delta}(\mathbf{x}_a^*, \mathbf{x}_b^*) = c^\delta(\mathbf{x}_a^*, \mathbf{x}_b^*) - \mathbf{r}^\delta(\mathbf{x}_a^*)^T (\mathbf{R}^\delta)^{-1} \mathbf{r}^\delta(\mathbf{x}_b^*). \quad (13)$$

It is clear that $\delta(\cdot) | \Theta$ and $\delta(\cdot) | \delta_z, \Theta$ are both GaSPs with different means and covariance functions. We have the following lemma for computing the density in (11).

Lemma 1. For any $\delta(\cdot) \sim \text{GaSP}(\mu(\cdot), \sigma^2 c(\cdot, \cdot))$ defined on \mathcal{X} , if $\|\mu(\cdot)\|_{L_2(\mathcal{X})} < \infty$, one has

$$\int_{\mathbf{x} \in \mathcal{X}} \delta(\mathbf{x})^2 d\mathbf{x} \sim \sigma^2 \sum_{i=1}^{\infty} \lambda_i \chi_{a_i}^2(1),$$

where $\chi_{a_i}^2(1)$ is a non-central chi-squared distribution with 1 degree of freedom and the non-central parameter $a_i = \mu_i^2 / (\lambda_i \sigma^2)$ with $\mu_i = \int_{\mathbf{x} \in \mathcal{X}} \mu(\mathbf{x}) \phi_i(\mathbf{x}) d\mathbf{x}$, λ_i being the i^{th} eigenvalue and ϕ_i being the i^{th} normalized eigenfunction of $c(\cdot, \cdot)$ with regard to the Lebesgue measure.

Based on Lemma 1, both $p_\delta \left(\int_{\xi \in \mathcal{X}} \delta(\xi)^2 d\xi = z \mid \delta_z, \Theta \right)$ and $p_\delta \left(\int_{\xi \in \mathcal{X}} \delta(\xi)^2 d\xi = z \mid \Theta \right)$ in (11) are the densities of an infinite weighted sum of non-central chi-squared distributions, which can be approximated by discretization. Direct calculation of the densities of the weighted sum of chi-squared distributions, however, is computationally challenging and could lead to a large approximation error. Later we will introduce a more robust way to evaluate the likelihood of the S-GaSP model along with the reference choice of $p_Z(\cdot)$ in the following Section 2.2.

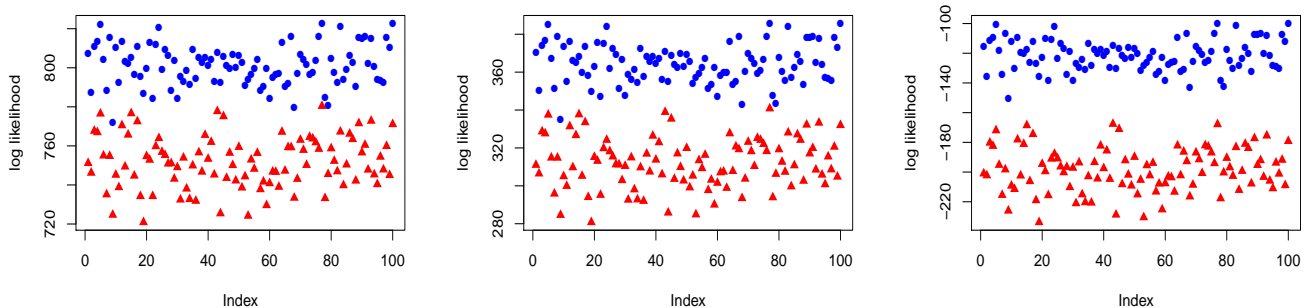


Figure 2: The log-likelihood function $\ell(\theta)$ at different values of correlation by the S-GaSP model defined in (5). Power exponential correlation function $\exp(-(|x_i - x_j|/\gamma^\delta)^{1.9})$ is used for $\gamma = \{1, 1/10, 1/100\}$ for the left, middle and right panels. One hundred simulations are implemented in each case with the blue dots being $\ell(\theta = 0)$ (true model) and the red triangles being $\ell(\theta = 1)$ (misspecified model). The reference choice of $p_Z(\cdot)$ in (14) and $f_Z(\cdot)$ in (18) is used with $\lambda = n/2$. The average difference of the log-likelihood between the true model and misspecified model is 49.59, 52.11 and 77.14 for the left, middle and right panels, respectively.

Figure 2 shows the log-likelihood of the S-GaSP model of the example discussed in Section 1.2. $n = 200$ observations are now sampled from a zero mean S-GaSP model in (5) with the reference choice of $p_Z(\cdot)$ in (14) and $f_Z(\cdot)$ in (18) introduced in Section 2.2. The computer model is still $f^M(x, \theta) = \theta$ with $\theta = 0$ and $\theta = 1$, representing the true and misspecified models, respectively. Assume $\mu^\delta(x) = 0$. Unlike the GaSP model, the log-likelihood of the S-GaSP model is much larger at $\theta = 0$ (true model), regardless of the choice of γ^δ . Even when $\gamma^\delta = 1$, meaning the correlation is strong, the difference between the true model and wrong model is 49.59 in term of

the log-likelihood. In comparison, when the data is sampled from the GaSP, the log-likelihood of the true model is only around 0.93 larger than the one of misspecified model in this scenario. As the information mainly comes from the likelihood function, the S-GaSP model allows one to identify the true model even if the data is strongly correlated.

2.2 Choice of $p_Z(\cdot)$

The pivotal part of the S-GaSP model is the measure of the random variable $Z = \int_{\xi \in \mathcal{X}} \delta(\xi)^2 d\xi$, which is also the L_2 loss between the reality and computer model. Unlike the L_2 calibration, we do not assume the model with the smallest L_2 loss is necessarily the single best model. Instead, we put a prior on all the values, but favor those with the smaller L_2 loss, since the L_2 loss is still a good indicator of a well calibrated computer model. On the other hand, the density for $Z = z$ in a GaSP model is $p_\delta(\int_{\xi \in \mathcal{X}} \delta(\xi)^2 d\xi = z | \Theta)$, which was widely used in the GaSP calibration approach (Kennedy and O'Hagan, 2001; Bayarri et al., 2007b,a; Qian and Wu, 2008; Liu et al., 2009). Therefore, To combine these two ideas, we define the reference choice of $p_Z(\cdot)$ as follows:

$$p_Z(z | \Theta) = \frac{f_Z(z | \Theta) p_\delta\left(\int_{\xi \in \mathcal{X}} \delta(\xi)^2 d\xi = z | \Theta\right)}{\int_0^\infty f_Z(t | \Theta) p_\delta\left(\int_{\xi \in \mathcal{X}} \delta(\xi)^2 d\xi = t | \Theta\right) dt}, \quad (14)$$

where $f_Z(z | \Theta)$ is a non-increasing function. In this specification, the density for Z is chosen to be proportional to the GaSP prior for Z (as it is used widely in the previous literature), but scaled by a scaling function $f_Z(\cdot | \Theta)$ to avoid the sample path deviating too much from zero. We present the following lemma that connects the S-GaSP calibration and GaSP calibration.

Lemma 2 (Connection between the GaSP and S-GaSP model). *When $p_Z(\cdot)$ is defined in (14) and $f_Z(z | \Theta)$ is a non-zero constant for all $z \in [0, +\infty)$, the S-GaSP defined in (5) becomes the calibration model in (1) where $\delta(\cdot) \sim \text{GaSP}(\mu^\delta(\cdot), \sigma_\delta^2 c^\delta(\cdot, \cdot))$ and $\epsilon \sim N(0, \sigma_0^2)$.*

With the assumption in (14), the marginal density for any δ_z in the S-GaSP model in (11) becomes

$$p_{\delta_z}(\delta_z | \Theta) = \frac{b_1(\delta_z, \Theta)}{b_0(\Theta)} p_\delta(\delta_z | \Theta), \quad (15)$$

where

$$b_0(\Theta) = \int_0^\infty p_\delta\left(\int_{\xi \in \mathcal{X}} \delta(\xi)^2 d\xi = t | \Theta\right) f_Z(t | \Theta) dt, \quad (16)$$

$$b_1(\delta_z, \Theta) = \int_0^\infty p_\delta\left(\int_{\xi \in \mathcal{X}} \delta(\xi)^2 d\xi = z | \delta_z, \Theta\right) f_Z(z | \Theta) dz. \quad (17)$$

The $p_\delta(\delta_z | \Theta)$ is the likelihood by the GaSP model and $b_1(\delta_z, \Theta)/b_0(\Theta)$ is the weight depending on the choice of $f_Z(\cdot)$. The motivation is to give the higher weight to the θ that leads to the smaller L_2 loss conditional on the observations and other parameters.

For any proper density $f_Z(\cdot)$, one can use a Monte Carlo approach to calculate $b_0(\Theta)$ and $b_1(\delta_z, \Theta)$. To illustrate, one can first draw M samples z_i from $p_\delta\left(\int_{\xi \in \mathcal{X}} \delta(\xi)^2 d\xi = z | \delta_z, \Theta\right)$ using

Lemma 1, and then compute $\sum_{i=1}^M f_Z(z_i | \Theta)/M$ to approximate $b_1(\boldsymbol{\delta}_z, \Theta)$. The same strategy applies to $b_0(\Theta)$. This provides a comparatively more stable way in evaluating the likelihood in the S-GaSP model than directly computing the density of the weighted sum of the chi-squared distributions discussed in the Section 2.1.

For the demonstration purpose and computational reason, we use the following exponential distribution for $f_Z(\cdot)$,

$$f_Z(z | \Theta) = \frac{\lambda}{2\sigma_\delta^2 \text{Vol}(\mathcal{X})} \exp\left(-\frac{\lambda z}{2\sigma_\delta^2 \text{Vol}(\mathcal{X})}\right), \quad (18)$$

where λ is a positive scaling parameter and $\text{Vol}(\mathcal{X})$ is the volume of \mathcal{X} . A larger λ favors the sample function with a smaller L_2 norm, while a smaller λ means the S-GaSP model is closer to a GaSP model. The magnitude of λ determines how similar the S-GaSP model is to these two approaches.

With the specification of $f_Z(\cdot)$ in (18), the S-GaSP becomes the GaSP with a transformed kernel function, stated in the following lemma.

Lemma 3 (Marginal distribution of the S-GaSP model). *Assume $p_Z(z | \Theta)$ follows the form (14) and $f_Z(\cdot)$ is specified in (18). The marginal distribution of $\boldsymbol{\delta}_z = (\delta_z(\mathbf{x}_1), \dots, \delta_z(\mathbf{x}_n))^T$ induced by the S-GaSP defined in (5) follows a multivariate normal distribution*

$$\boldsymbol{\delta}_z | \Theta \sim MN(\mathbf{0}, \sigma_\delta^2 \mathbf{R}_z), \quad (19)$$

where the covariance follows

$$\mathbf{R}_z = (\mathbf{B} + (\mathbf{R}^\delta)^{-1})^{-1}, \quad (20)$$

and \mathbf{B} is an $n \times n$ finite real-valued matrix with the following form

$$\mathbf{B} = (\mathbf{R}^\delta)^{-1} \left\{ \sum_{i=1}^{\infty} \frac{\lambda}{\text{Vol}(\mathcal{X}) + \lambda_i^* \lambda} \left(\int_{\mathbf{x} \in \mathcal{X}} \mathbf{r}^\delta(\mathbf{x}) \phi_i^*(\mathbf{x}) d\mathbf{x} \right) \left(\int_{\mathbf{x} \in \mathcal{X}} \mathbf{r}^\delta(\mathbf{x}) \phi_i^*(\mathbf{x}) d\mathbf{x} \right)^T \right\} (\mathbf{R}^\delta)^{-1}, \quad (21)$$

with λ_i^* and $\phi_i^*(\mathbf{x})$ being the i^{th} eigenvalue and normalized eigenfunction of $c^{*\delta}(\cdot, \cdot)$ defined in (13) with regard to the Lebesgue measure, respectively.

By Lemma 3, $\boldsymbol{\delta}_z$ can be marginalized out, and the resulting marginal distribution of $\mathbf{y}^F = (y^F(\mathbf{x}_1), \dots, y^F(\mathbf{x}_n))^T$ is still a multivariate normal distribution. Such simplification relies on the reference choice of $p_Z(\cdot)$ in (14) and $f_Z(\cdot)$ in (18), which allows us to avoid the Monte Carlo method for computing the likelihood. To calculate the marginal distribution in (19), however, requires the discretization of the integral, which can still be quite complicated (especially when prediction at many unobserved points is one of the goals). We further provide an extremely simple way for the computation, discussed in the following subsection.

2.3 S-GaSP model with constraints on finite points

This subsection handles the issue of discretization of the S-GaSP model in (5). We use N_C distinct points \mathbf{x}_i^C to discretize \mathcal{X} for $i = 1, \dots, N_C$, such that $\int_{\boldsymbol{\xi} \in \mathcal{X}} \delta(\boldsymbol{\xi})^2 d\boldsymbol{\xi} \approx \sum_{i=1}^{N_C} \delta(\mathbf{x}_i^C)^2 \Delta x$, with

$\Delta x = \text{Vol}(\mathcal{X})/N_C$ and $\text{Vol}(\mathcal{X})$ being the volume of \mathcal{X} . We are ready to define the S-GaSP model on finitely many constraint points as follows:

$$\begin{aligned} y^F(\mathbf{x}) &= f^M(\mathbf{x}, \boldsymbol{\theta}) + \mu^\delta(\mathbf{x}) + \delta_Z^a(\mathbf{x}) + \epsilon, \\ \delta_Z^a(\mathbf{x}) &= \left\{ \delta(\mathbf{x}) \mid \sum_{i=1}^{N_C} \delta(\mathbf{x}_i^C)^2 \Delta x = Z \right\}, \\ \delta(\cdot) &\sim \text{GaSP}(0, \sigma_\delta^2 c^\delta(\cdot, \cdot)), \\ Z &\sim p_Z(\cdot), \epsilon \sim N(0, \sigma_0^2). \end{aligned} \tag{22}$$

We call (22) the approximate S-GaSP model, where the only approximation is to discretize the integral in the S-GaSP model in (5). To choose adequate constraint points could be challenging, especially when the dimension of \mathbf{x} is large. A convenient choice is to let $\mathbf{x}_i^C = \mathbf{x}_i$, in which case if the design of the experiments follows a “space-filling” scheme, $\sum_{i=1}^{N_C} \delta(\mathbf{x}_i^C)^2 \Delta x \approx \int_{\boldsymbol{\xi} \in \mathcal{X}} \delta(\boldsymbol{\xi})^2 d\boldsymbol{\xi}$ when the number of design points is large. We are able to show that under the reference choice of the scaling density $p_Z(\cdot)$, the marginal distribution of the discrepancy at any set of variable inputs is a multivariate normal distribution in the approximate S-GaSP model.

Lemma 4 (Marginal distribution of the approximate S-GaSP model). *Assume $p_Z(z \mid \boldsymbol{\Theta})$ follows the form (14) and $f_Z(\cdot)$ is specified in (18). The marginal distribution of $\boldsymbol{\delta}_z^a = (\delta_z^a(\mathbf{x}_1), \dots, \delta_z^a(\mathbf{x}_n))^T$ in the approximate S-GaSP in (22) follows a multivariate normal distribution*

$$\boldsymbol{\delta}_z^a \mid \boldsymbol{\Theta} \sim MN(\mathbf{0}, \sigma_\delta^2 \mathbf{R}_z^a), \tag{23}$$

where

$$\mathbf{R}_z^a = \mathbf{R}^\delta - (\mathbf{r}^C)^T \left(\mathbf{R}^C + \frac{N_C}{\lambda} \mathbf{I}_{N_C} \right)^{-1} \mathbf{r}^C. \tag{24}$$

with \mathbf{R}^C being an $N_C \times N_C$ correlation matrix between constraint points with the (i, j) entry $\mathbf{R}_{i,j}^C = c^\delta(\mathbf{x}_i^C, \mathbf{x}_j^C)$; \mathbf{r}^C being an $N_C \times n$ correlation matrix between constraint points and observed points with the (i, j) entry being $r_{i,j}^C = c^\delta(\mathbf{x}_i^C, \mathbf{x}_j)$.

Lemma 4 is important for computation. Note that computing the marginal distribution at $\boldsymbol{\delta}_z^a$ in the S-GaSP model does not require the Monte Carlo method and does not even require to compute the eigenvectors or eigenvalues of the correlation matrix. With such simplification, one can marginalize out $\delta_Z^a(\cdot)$ to obtain the marginal distribution of the field data.

Theorem 1 (Marginal distribution of the field data). *Assume the conditions of Lemma 4 hold. After marginalizing out $\delta_Z^a(\cdot)$, the marginal likelihood of $\mathbf{y}^F = (y^F(\mathbf{x}_1), \dots, y^F(\mathbf{x}_n))^T$ defined in the approximate S-GaSP model in (22) follows*

$$\mathbf{y}^F \mid \boldsymbol{\Theta} \sim MN(\mathbf{f}^M(\mathbf{x}_{1:n}, \boldsymbol{\theta}) + \boldsymbol{\mu}^\delta, \sigma_\delta^2 \mathbf{R}_z^a + \sigma_0^2 \mathbf{I}_n), \tag{25}$$

where $\mathbf{f}^M(\mathbf{x}_{1:n}, \boldsymbol{\theta}) = (f^M(\mathbf{x}_1, \boldsymbol{\theta}), \dots, f^M(\mathbf{x}_n, \boldsymbol{\theta}))^T$ are the computer model outputs evaluated at \mathbf{x}_i and $\boldsymbol{\theta}$, $i = 1, \dots, n$; the mean discrepancy is $\boldsymbol{\mu}^\delta = (\mu^\delta(\mathbf{x}_1), \dots, \mu^\delta(\mathbf{x}_n))^T$ with each term defined in (6) and the correlation matrix \mathbf{R}_z^a of the discrepancy function is defined in (24).

Theorem 1 can be directly shown using Lemma 4 and the property of the multivariate normal distribution. Conditional on all other parameters, the predictive distribution for $y^F(\mathbf{x}^*)$ combining the calibrated computer model and discrepancy function is given in the following Theorem.

Theorem 2 (Predictive distribution). *Assume the conditions of Lemma 4 hold. The predictive distribution of the field data at a new points \mathbf{x}^* by the approximate S-GaSP model in (22) follows*

$$y^F(\mathbf{x}^*) \mid \mathbf{y}^F, \Theta \sim N(\hat{\mu}(\mathbf{x}^*), \sigma_\delta^2 c^* + \sigma_0^2),$$

where

$$\begin{aligned} \hat{\mu}(\mathbf{x}^*) &= f^M(\mathbf{x}^*, \boldsymbol{\theta}) + \mu^\delta(\mathbf{x}^*) + \mathbf{r}_z^a(\mathbf{x}^*)^T (\tilde{\mathbf{R}}_z^a)^{-1} (\mathbf{y}^F - \mathbf{f}^M(\mathbf{x}_{1:n}, \boldsymbol{\theta}) - \boldsymbol{\mu}^\delta), \\ c^* &= c_z^a(\mathbf{x}^*, \mathbf{x}^*) - \mathbf{r}_z^a(\mathbf{x}^*)^T (\tilde{\mathbf{R}}_z^a)^{-1} \mathbf{r}_z^a(\mathbf{x}^*), \end{aligned}$$

with $\tilde{\mathbf{R}}_z^a = \mathbf{R}_z^a + \sigma_0^2 \mathbf{I}_n / \sigma_\delta^2$, $\mathbf{r}_z^a(\mathbf{x}^*) = \mathbf{r}_z^\delta(\mathbf{x}^*) - (\mathbf{r}^C)^T (\tilde{\mathbf{R}}^C)^{-1} \mathbf{r}^C(\mathbf{x}^*)$, $\mathbf{r}^C(\mathbf{x}^*) = (c^\delta(\mathbf{x}_1^C, \mathbf{x}^*), \dots, c^\delta(\mathbf{x}_{N_C}^C, \mathbf{x}^*))^T$, $c_z^a(\mathbf{x}^*, \mathbf{x}^*) = c^\delta(\mathbf{x}^*, \mathbf{x}^*) - \mathbf{r}^C(\mathbf{x}^*)^T (\tilde{\mathbf{R}}^C)^{-1} \mathbf{r}^C(\mathbf{x}^*)$, and $\tilde{\mathbf{R}}^C = \mathbf{R}^C + N_C \mathbf{I}_{N_C} / \lambda$.

Theorem 2 can be checked easily using Theorem 1 and the property of the multivariate normal distribution. Both the marginal distribution and predictive distribution can be computed easily given a set of parameters.

Figure 3 and Figure 4 compare the prediction by the GaSP and S-GaSP models for two nonlinear functions. Both models perform reasonably well with limited amount of input values sampled from the maxmin Latin hypercube design (Santner et al., 2013), which suggests that both models serve as a good sampling model for complicated nonlinear functions. In Figure 2, we have shown that the true model can be identified from the S-GaSP calibration with the reference choice of the scaling density, even when the correlation is strong in the data. Here the prediction results shown in Figure 3 and Figure 4 suggest that such choice does not result in a loss of predictive power in the S-GaSP model, as the S-GaSP and GaSP models predict equally well in these examples.

2.4 Parameter estimation and computation

Here we introduce a Bayesian paradigm to assess the parameters uncertainty in both GaSP and S-GaSP model. The shared parameters in both models are $\Theta = [\boldsymbol{\theta}; \boldsymbol{\beta}^\delta; \boldsymbol{\gamma}^\delta; \sigma_\delta^2; \sigma_0^2]$. We first do a transformation to define a nugget-variance ratio parameter $\eta = \sigma_0^2 / \sigma_\delta^2$ and inverse range parameter $\boldsymbol{\psi}^\delta = 1 / \boldsymbol{\gamma}^\delta$. The transformed parameters are then $\tilde{\Theta} = [\boldsymbol{\theta}; \boldsymbol{\beta}^\delta; \boldsymbol{\psi}^\delta; \sigma_\delta^2; \eta]$. We assume the prior for $\tilde{\Theta}$ has the following form

$$\pi(\tilde{\Theta}) \propto \frac{\pi(\boldsymbol{\theta}) \pi(\boldsymbol{\psi}^\delta, \eta) \pi(\lambda)}{\sigma_\delta^2}, \quad (26)$$

where $\pi(\boldsymbol{\theta})$ and $\pi(\boldsymbol{\psi}^\delta, \eta)$ are the prior for the calibration parameters and the prior for the inverse range and the nugget parameters, both being proper distributions.

The prior for $\boldsymbol{\theta}$ should be chosen based on expert knowledge, as these parameters have real meanings in a computer model. Thus, we do not introduce any specific form herein. The objective priors of the parameters in the covariance matrix in the GaSP model have been studied extensively (see e.g. Berger et al. (2001); De Oliveira (2007); Ren et al. (2012); Paulo (2005); Gu and Berger

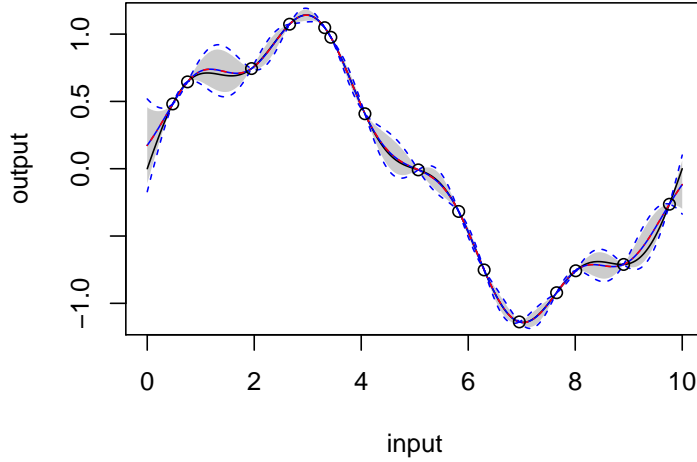


Figure 3: Comparison of the prediction by the GaSP and S-GaSP models for a one dimensional function (Higdon et al., 2002). The true function is $y = \sin(2\pi x/10) + 0.2 \sin(2\pi x/2.5)$, graphed as the black curve. 15 training values of the function are plotted as black circles. The predictive mean of the GaSP and S-GaSP models overlaps and is graphed as the red dotted curve and blue solid curve, respectively. The shaded area is the 95% predictive interval by the GaSP model and the area between two blue dotted curves is the 95% predictive interval by the S-GaSP model. Both models take a constant mean and Matérn correlation in (10) with the range parameter estimated by the RobustGaSP R package (Gu et al., 2016b). The reference choice of $p_Z(\cdot)$ in (14) and $f_Z(\cdot)$ in (18) of the S-GaSP model is used with $\lambda = n/2$. The mean squared predictive errors for the GaSP and S-GaSP are 7.54×10^{-4} and 7.56×10^{-4} , respectively.

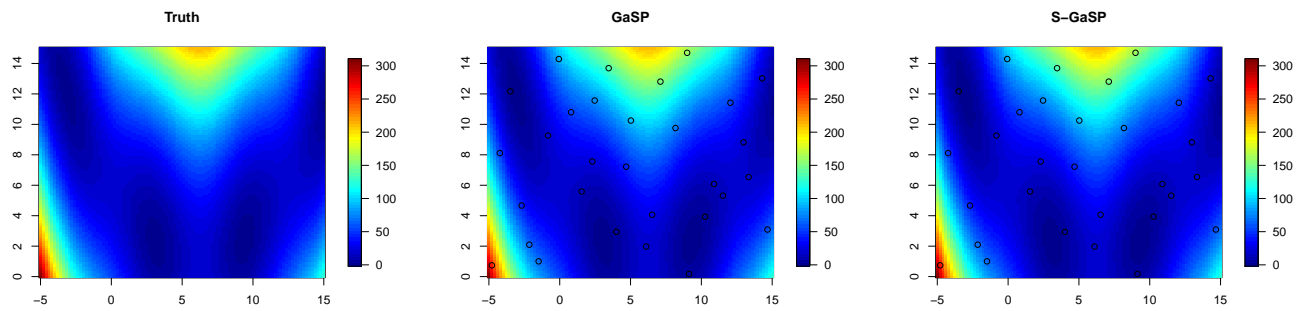


Figure 4: Prediction of the GaSP and S-GaSP for the Brainin function (Forrester et al., 2008). 30 training values of function are plotted as black circles. Both models take a constant mean and Matérn correlation in (10) with the range parameter estimated by the RobustGaSP R package (Gu et al., 2016b). The reference choice of $p_Z(\cdot)$ in (14) and $f_Z(\cdot)$ in (18) of the S-GaSP model is used with $\lambda = n/2$. The mean squared predictive errors for the GaSP and S-GaSP are 0.659 and 0.587, respectively.

(2017)). However the objective priors for the S-GaSP model have not been studied. Here we use the jointly robust prior with the following form for the demonstration purpose

$$\pi(\boldsymbol{\psi}^\delta, \eta) \propto \left(\sum_{i=1}^{p_x} C_i \psi_i^\delta + \eta \right)^a \exp \left(-b \left(\sum_{i=1}^{p_x} C_i \psi_i^\delta + \eta \right) \right),$$

with a, b, C_i being the prior parameters, for $i = 1, \dots, p_x$. The jointly robust prior was first introduced in Gu (2016) to match the tail rates of the reference prior. It is a proper prior and has a closed-form normalizing constant, prior mean and variance. The default choice of the prior parameters for a rectangle \mathcal{X} are $C_i = |\mathcal{X}_i| n^{-1/p_x}$, with $|\mathcal{X}_i|$ being the length of the space of the i^{th} dimension of the variable input, $a = 1/2 - p_x$ and $b = 1$.

In the S-GaSP model, the parameter λ controls how similar the process to the GaSP model. In all the numerical studies, we let the constraint points be the observed data, i.e. $\mathbf{x}_i^C = \mathbf{x}_i$, for $i = 1, \dots, n$, and $\lambda = n/2$ with n being the number of observations. Such choice is ad-hoc but seems to perform reasonably well in calibration. One may develop a prior for the uncertainty in λ , but we do not explore in this direction.

We utilize a Metropolis Hasting algorithm to sample from the posterior with the likelihood of the observations in (25) and the prior in (26). Compared to a GaSP model, the added computational operations are on the computation of \mathbf{R}_z , which is at the order of $O(N_C^3)$ and $O(nN_C^2)$ due to matrix inversion and multiplication. The default choice of the constraint points is to let $\mathbf{x}_i^C = \mathbf{x}_i$, in which case the added computation is $O(n^3)$, the same as the computational operations in the GaSP model.

2.5 Comparison to the orthogonal Gaussian stochastic process

In this subsection, we compare our S-GaSP model to a recent approach, called the orthogonal Gaussian stochastic process (orthogonal GaSP) introduced in Plumlee (2016). Under some regularity conditions of $f^M(\cdot, \cdot)$ and assuming the existence and uniqueness of the L_2 minimizer, $\boldsymbol{\theta}_{L_2}$, it is recently shown in Plumlee (2016) that the following constraint on the discrepancy function holds

$$\int_{\mathbf{x} \in \mathcal{X}} D^{(0,1)} f^M(\mathbf{x}, \boldsymbol{\theta}^*) \delta(\mathbf{x}) d\mathbf{x} = \mathbf{0}, \quad (27)$$

where $D^{(0,1)} f^M(\mathbf{x}, \boldsymbol{\theta}_{L_2})$ is the derivative of $f^M(\cdot, \cdot)$ with regard to $\boldsymbol{\theta}$, evaluated at \mathbf{x} and $\boldsymbol{\theta} = \boldsymbol{\theta}_{L_2}$. In Plumlee (2016), it is also shown that if the discrepancy is modeled by a zero-mean orthogonal GaSP for any $\mathbf{x}, \mathbf{x}' \in \mathcal{X}$

$$\delta_{O-GaSP}(\cdot) \sim \text{GaSP}(0, \sigma_\delta^2 c_{O-GaSP}^\delta(\cdot, \cdot)),$$

where

$$c_{O-GaSP}^\delta(\mathbf{x}, \mathbf{x}') = c^\delta(\mathbf{x}, \mathbf{x}') - g_{O-GaSP}(\mathbf{x})^T G_{O-GaSP}^{-1} g_{O-GaSP}(\mathbf{x}'), \quad (28)$$

for any positive definite covariance function $c^\delta(\mathbf{x}, \mathbf{x}')$ with

$$g_{O-GaSP}(\mathbf{x}) = \int_{\boldsymbol{\xi} \in \mathcal{X}} D^{(0,1)} f^M(\boldsymbol{\xi}, \boldsymbol{\theta}) c^\delta(\mathbf{x}, \boldsymbol{\xi}) d\boldsymbol{\xi},$$

and

$$G_{O-GaSP} = \int_{\xi' \in \mathcal{X}} \int_{\xi \in \mathcal{X}} D^{(0,1)} f^M(\xi, \theta) [D^{(0,1)} f^M(\xi', \theta)]^T c^\delta(\xi, \xi') d\xi d\xi',$$

the (27) holds with probability 1.

We denote $\delta_{O-GaSP}(\cdot)$ as the orthogonal GaSP for modeling the discrepancy function. The sample path of $\delta_{O-GaSP}(\cdot)$ has to satisfy (27). However, as in the case of all the optimization problems, (27) holds not only for the L_2 minimizer, θ_{L_2} , but also for many other θ . In particular, any local maximum of the L_2 norm of the discrepancy function also satisfies the constraints in (27), which makes the likelihood function favor the local maximizers as well. As $f^M(\mathbf{x}, \theta)$ is typically a nonlinear function of θ , the L_2 loss function is often multi-dimensional and likely to have multiple extreme values in reality. It is obviously unreasonable to favor the local maximizers of L_2 loss. A numerical example between the S-GaSP and the orthogonal GaSP calibration is given in Section 4.1.

3 Calibration and prediction for slow computer models

This section handles the issue when the computer model is computationally expensive to evaluate. When the computer model is slow, the common approach is to use an emulator, i.e., a statistical model that can accurately approximate the computer model and can be run very fast. Using a GaSP model as the emulator is well-studied in recent literature (Sacks et al., 1989; Bayarri et al., 2009; Spiller et al., 2014; Gu et al., 2016a). To begin with, we first run the computer model on D design points, denoted as $((\mathbf{x}_1^{\mathcal{D}}, \theta_1^{\mathcal{D}}); \dots; (\mathbf{x}_D^{\mathcal{D}}, \theta_D^{\mathcal{D}}))$. The design is typically chosen to fill the input space and one of the frequently used approaches is the Latin hypercube design (Santner et al., 2013). Let $(f^M(\mathbf{x}_1^{\mathcal{D}}, \theta_1^{\mathcal{D}}), \dots, f^M(\mathbf{x}_D^{\mathcal{D}}, \theta_D^{\mathcal{D}}))^T$ be the simulator outputs at the design points. The emulator models $f^M(\cdot, \cdot)$ as an unknown function by the GaSP model. For any (\mathbf{x}, θ) , the mean function is still modeled via regression

$$\mu^M(\mathbf{x}, \theta) = \mathbf{h}^M(\mathbf{x}, \theta) \boldsymbol{\beta}^M = \sum_{i=1}^{q_M} h_i^M(\mathbf{x}, \theta) \beta_i^M,$$

where $\mathbf{h}^M(\mathbf{x}, \theta) = (h_1^M(\mathbf{x}, \theta), \dots, h_{q_M}^M(\mathbf{x}, \theta))$ is the mean basis function and β_i^M is the i^{th} regression parameter for $h_i^M(\mathbf{x}, \theta)$, $i = 1, \dots, q_M$. For any two inputs (\mathbf{x}_a, θ_a) and (\mathbf{x}_b, θ_b) , the correlation is again assumed to have a product form

$$c^M((\mathbf{x}_a, \theta_a), (\mathbf{x}_b, \theta_b)) = \prod_{i=1}^{p_x} c_i^M(x_{ai}, x_{bi}) \prod_{j=1}^{p_\theta} c_j^M(\theta_{aj}, \theta_{bj}), \quad (29)$$

where $c_i^M(x_{ai}, x_{bi})$ and $c_j^M(\theta_{aj}, \theta_{bj})$ are one-dimensional correlation functions, for $i = 1, \dots, p_x$ and $j = 1, \dots, p_\theta$.

The parameters in the GaSP emulator are $(\sigma_M^2, \boldsymbol{\beta}^M, \boldsymbol{\gamma}^M)$. To explore the uncertainty in these parameters, a full Bayesian approach would combine the emulator into the calibration model (5). However, the field data is typically much noisier than the computer model outputs and provides no information in emulating the computer model. Combining the emulator and calibration model may also cause additional identifiability issues (Bayarri et al., 2007b). To overcome these issues,

a modular approach is often assumed (Liu et al., 2009), meaning that the uncertainty of the parameters in the emulator is handled using only outputs from the computer model.

Estimating the parameters in an emulator is not trivial, and some routinely used estimators, such as the maximum likelihood estimator, have been widely recognized to be unstable in previous studies (Oakley, 1999; Li and Sudjianto, 2005; Lopes, 2011). We assume an objective prior for the parameters in the GaSP emulator, $\pi(\sigma_M^2, \boldsymbol{\beta}^M, \boldsymbol{\gamma}^M) \propto \pi^R(\boldsymbol{\gamma}^M)/\sigma_M^2$, where $\pi^R(\boldsymbol{\gamma}^M)$ is the reference prior for the range parameters (Berger et al., 2001; Paulo, 2005). σ_M^2 and $\boldsymbol{\beta}^M$ can be marginalized out analytically, and $\boldsymbol{\gamma}^M$ is estimated by the marginal posterior mode with the robust parameterization (Gu and Berger, 2017). The resulting predictive distribution at any new point $(\mathbf{x}^*, \boldsymbol{\theta}^*)$ follows a Student’s t-distribution. We omit the details of implementing the emulator due to the limitation of the space. The theoretical justification of the emulator is discussed in Gu and Berger (2017), and the resulting GaSP emulator is implemented in the R package (Gu et al., 2016b). In the calibration stage, we draw from the posterior predictive distribution $p(f^M(\mathbf{x}^*, \boldsymbol{\theta}^*) | f^M(\mathbf{x}_1^{\mathcal{D}}, \boldsymbol{\theta}_1^{\mathcal{D}}), \dots, f^M(\mathbf{x}_D^{\mathcal{D}}, \boldsymbol{\theta}_D^{\mathcal{D}}))$ when we need to evaluate an computationally expensive computer model at $(\mathbf{x}^*, \boldsymbol{\theta}^*)$.

4 Numerical comparison

In this section, we provide numerical comparisons among several approaches for calibration and prediction. To maintain a fair comparison, the mean function, covariance function, prior distribution as well as initial values in the MCMC algorithm are all set to be the same. We further let the acceptance rate in the MCMC be close to 1/3. The correlation function is assumed to have the product form as in (8), where each one-dimension correlation function is defined by (10), and the prior is assumed to have a product form in expression (26). The uniform prior for $\boldsymbol{\theta}$ is used and the mean discrepancy is set to be 0, i.e. $\mu^\delta(\mathbf{x}) = 0$.

We first compare the GaSP and S-GaSP models to the orthogonal GaSP model for an example in Section 4.1. A real example using satellite images for calibrating a geophysical model for the Kilauea Volcano is studied in Section 4.2. In both examples, $S = 50,000$ posterior samples of the parameters $\tilde{\boldsymbol{\Theta}} = (\boldsymbol{\theta}, \boldsymbol{\beta}^\delta, \boldsymbol{\psi}^\delta, \sigma_\delta^2, \eta)$ in the GaSP and S-GaSP calibration are generated with the first $S_0 = 5,000$ being used as the burn-in samples. The results are then analyzed based on these posterior samples.

4.1 Simulated example: a multi-modal L_2 loss function

We first consider an example where the L_2 loss function contains multiple extreme values.

Example 1. Suppose $y^F(x) = x \cos(3x/2) + x + \epsilon$ with $x \in [0, 5]$ and $\epsilon \sim N(0, 0.2^2)$. Assume the computer model is $f^M(x, \theta) = \sin(\theta x) + x$ for $\theta \in [0, 3]$.

The target function and computer model with two different choices of θ in Example 1 are plotted in the upper left panel in Figure 5. The L_2 loss function over $\theta \in [0, 3]$ is graphed in the upper right panel in Figure 5, which contains the global minimum at $\theta \approx 1.88$, a local minimum at $\theta \approx 0.26$ and two local maxima at $\theta \approx 1.06$ and $\theta \approx 2.62$, respectively.

Assume one obtains 15 observations, denoted as $y^F(x_i)$, for $i = 1, \dots, 15$, equally spaced in $[0, 5]$. The log-likelihood of GaSP, S-GaSP and orthogonal GaSP models is plotted in the lower

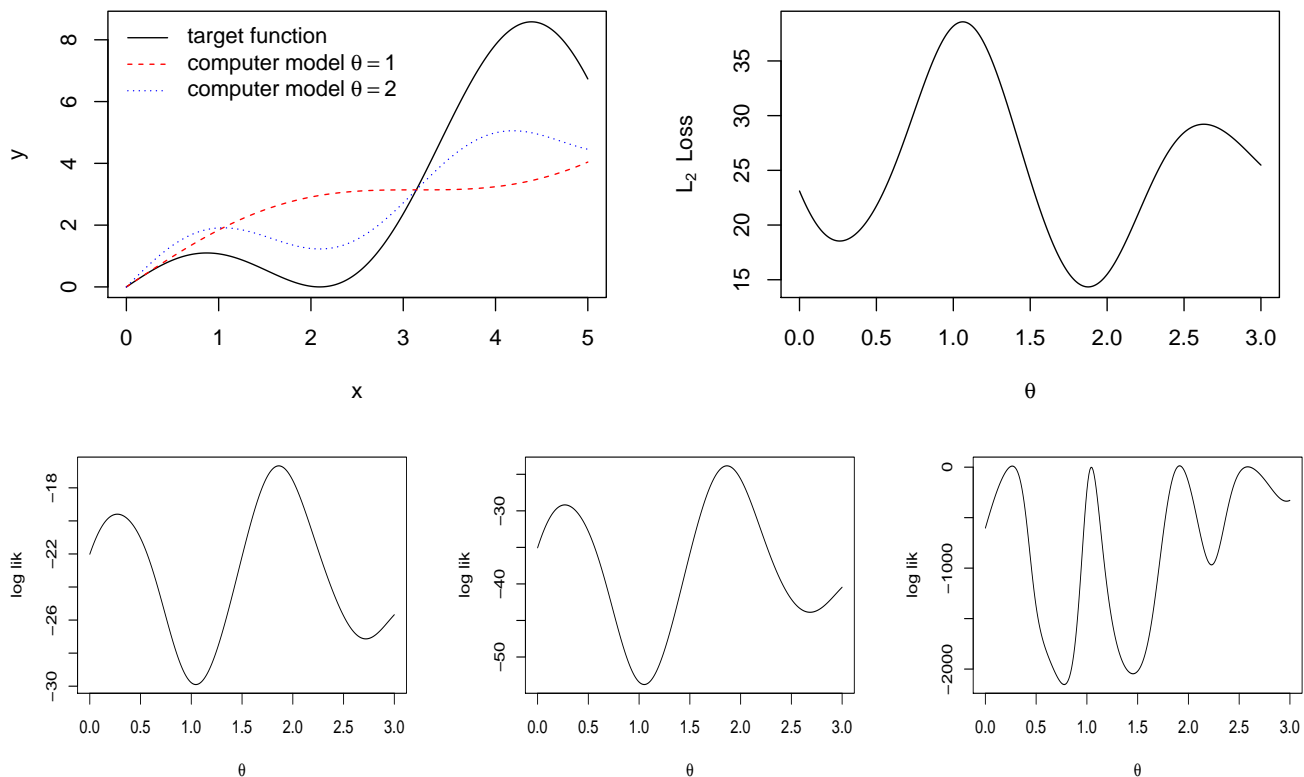


Figure 5: The target function, computer model outputs at two different values and the L_2 loss function in Example 1 are graphed in the first row. The log-likelihood of the GaSP (left), S-GaSP (middle) and orthogonal GaSP (right) is graphed in the left, middle, and right panels in the second row, respectively. For all models, the Matérn covariance in (10) with $\sigma_\delta^2 = 1$, $\gamma^\delta = 1/2$ and $\eta = 0.01$ is used.

left, middle and right panels in Figure 5, respectively. Not surprisingly, the log-likelihood of the orthogonal GaSP model has modes at all the extreme values in the L_2 loss function, including both local minima and maxima. Note that this phenomenon is not caused by the choice of the covariance function, but by the constraint in (27). Since all the extreme values in the L_2 loss function satisfy this constraint, the likelihood function of the orthogonal GaSP model is inevitably large at the extreme values as a consequence. Unlike the orthogonal GaSP model, the information in the L_2 loss is faithfully expressed in the GaSP and S-GaSP models.

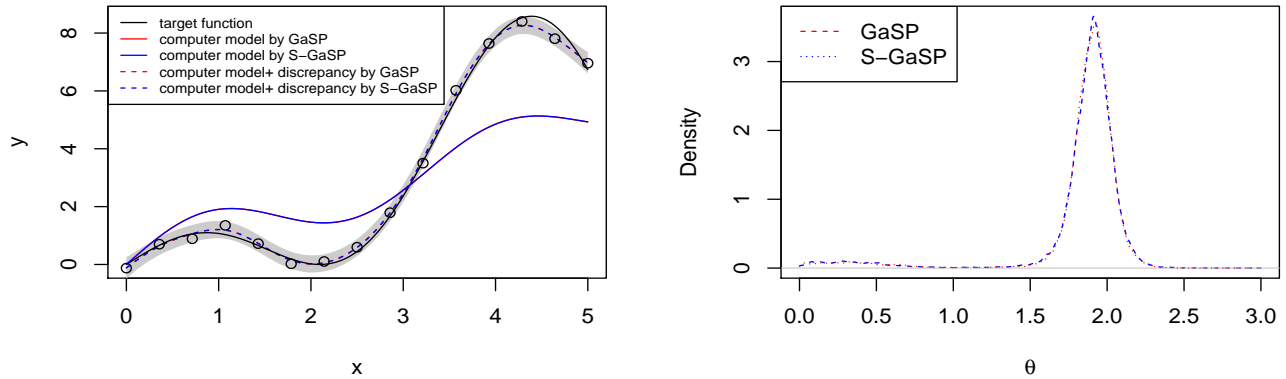


Figure 6: The comparison between the GaSP and S-GaSP models for Example 1. In the left panel, the target function is plotted as the black solid curve, and 15 noisy observations equally spaced in $[0, 5]$ are plotted as black circles. The predictive mean by the GaSP and S-GaSP models is graphed as the red dashed curve and blue dotted curve, respectively. The right panel shows the marginal posterior densities by the default density estimation in R based on the posterior samples by the GaSP model (dashed curve) and S-GaSP model (dotted curve). The blue curve and red curve overlap in both panels.

Although Example 1 is artificial, this scenario is not unusual in real applications, where θ is often multi-dimensional and the L_2 loss function is likely to have multiple extreme values. Sometimes an informative prior of θ could help to distinguish the local extreme values. However, the likelihood function shown in Figure 5 by the orthogonal GaSP model is undesirable, as there is no reason for the likelihood function to favor those local maxima in terms of the L_2 loss function. To overcome the issue caused by the local maxima in the L_2 loss function, one could possibly explore the second-order optimality condition of the L_2 loss function with regard to θ . However, such extension is complicated, as there are p_x^2 inequality constraints on the Hessian matrix. It also may not be feasible in practice, as some computer models do not even have the second derivative. Thus precaution is needed when using the orthogonal GaSP model for calibration.

The out of sample predictions by the GaSP and S-GaSP models are shown in left panel in Figure 6. The predictions by the calibrated computer model are graphed as the red and blue solid curves by the GaSP model and S-GaSP model, respectively, while the dashed curves are the predictions by the calibrated computer model and discrepancy together. The predictions by both models overlap each other with or without the discrepancy. In this example, as the computer

model is not equal to the truth for any θ , the computer model that minimizes the L_2 loss still has a comparatively large error. Modeling a discrepancy function by either a GaSP model or an S-GaSP model clearly improves the predictions, even with only $n = 15$ observations.

The posterior distributions of θ by the GaSP and S-GaSP model are graphed as the red dashed curve and blue dotted curve in the right panel in Figure 6. Most of the posterior mass by both models are concentrated at the minimum of L_2 loss, meaning that GaSP, S-GaSP and L_2 calibration agree with each other in this example.

4.2 Real example: calibration of the geophysical model for the Kilauea Volcano

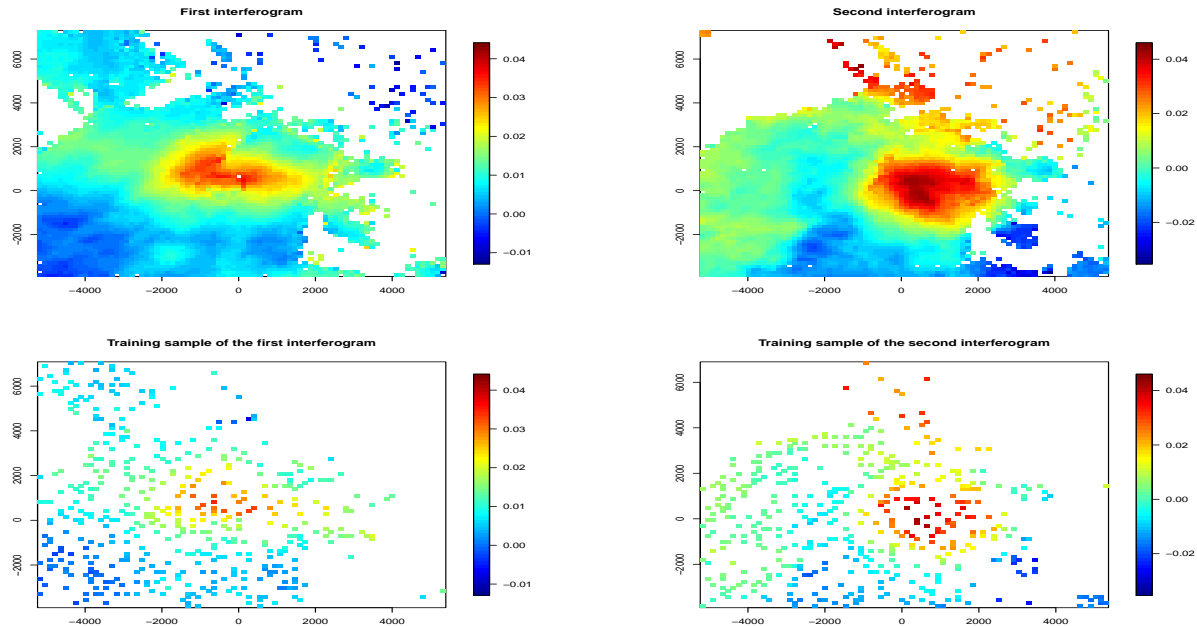


Figure 7: Two interferograms of Kilauea Volcano are graphed in the first row and 500 uniform samples for each interferogram are graphed in the second row.

In this subsection, we consider the geophysical model of Kilauea Volcano introduced in Anderson and Poland (2016, 2017) for the study of the magma supply rate for Kilauea and estimates of carbon concentrations in Earth’s mantle. Several different types of data were used in these studies, including the SO_2 , CO_2 emission data, and Interferometric synthetic aperture radar (InSAR) data, a radar technique to estimate the ground deformation in centimeters (Massonnet and Feigl, 1998). In Anderson and Poland (2016), the parameters in the geophysical model were estimated using the Bayesian method without assuming a discrepancy function to the geophysical model.

For the demonstration purpose, we limit ourselves to calibrating one part of the geophysical model in Anderson and Poland (2016) – the displacement of the ground’s surface caused by addition of magma to a spherical reservoir. We use one ascending-mode and one descending-mode COSMO-SkyMed interferogram shown in Anderson and Poland (2016), spanning the period of time from October 21, 2011 to May 16, 2012 and October 20, 2011 to May 15, 2012, respectively. These

interferograms are graphed in the first row in Figure 7, showing that the ground deformation caused by the volcano is between 0 to 4 centimeters during this period of time. As the number of pixels in the InSAR data is large, a Quadtree algorithm was used for downsampling before calibration in Anderson and Poland (2016). This method converts each interferogram to an image with only several hundred boxes, where the size of the box is small if the values within the box change rapidly, that is, where deformation gradients are high. The Quadtree algorithm is designed for visualization purposes, however, as it favors those area with high ground deformation, it may cause potential bias in the calibration. Here we uniformly sample 500 points from each interferogram and use them as our training data for the calibration and prediction. Two variable inputs and five calibration parameters of this geophysical model are provided in Table 1.

Table 1: Input variables and calibration parameters of the geophysical model for Kilauea Volcano in 2011 to 2012.

Input variable (\mathbf{x})	Name	Description
x_1	Latitude	Spatial coordinate
x_2	Longitude	Spatial coordinate
Parameter ($\boldsymbol{\theta}$)	Name	Description
$\theta_1 \in [-2000, 3000]$	Chamber east (m)	Spatial coordinate for the chamber
$\theta_2 \in [-2000, 5000]$	Chamber north (m)	Spatial coordinate for the chamber
$\theta_3 \in [500, 6000]$	Chamber depth (m)	Depth of the chamber
$\theta_4 \in [0, 0.15]$	Res. vol. change rate (m^3/s)	Volume change rate of the reservoir
$\theta_5 \in [0.25, 0.33]$	Poisson's ratio	Host rock property

The marginal posterior densities of $\boldsymbol{\theta}$ by the GaSP and S-GaSP calibration are graphed as the red and blue curves in Figure 8, respectively. The posterior mass of the GaSP spreads widely throughout its domain, and a geophysical model with a deep chamber and high volume change rate of the reservoir is preferred. The uncertainty of location of the chamber from the GaSP calibration also seems quite large. In comparison, the S-GaSP model has more posterior mass concentrated at a chamber around 2700 meters in depth with the reservoir volume change rate being around $0.06 m^3/s$, both of which are much smaller than the ones in the GaSP calibration. The posterior mass by the S-GaSP is closer to the results without assuming a discrepancy function studied in Anderson and Poland (2016), in which the chamber depth is reported to be around 2300 meters and the reservoir volume change rate is around $0.05 m^3/s$. The small difference between the results in the S-GaSP calibration and in Anderson and Poland (2016) is debatable; however, the GaSP calibration seems to prefer a geophysical model with the depth of the chamber being around 5000 meters.

The difference of the marginal posterior distributions between the GaSP and S-GaSP calibration results in a large difference in prediction by the calibrated geophysical model, shown in the upper panels in Figure 9 and Figure 10 for the first and second interferograms, respectively. As the calibrated geophysical model from the GaSP calibration has a deep chamber of the volcano, the ground deformation caused by this geophysical model is very small, with the maximum change in ground deformation being less than 2 centimeters. The predictive mean squared error by the GaSP calibration is 2.70×10^{-5} and 1.43×10^{-4} for the first and second interferograms, respectively. Alternatively, the maximum ground deformation reported in the S-GaSP calibration is around 3

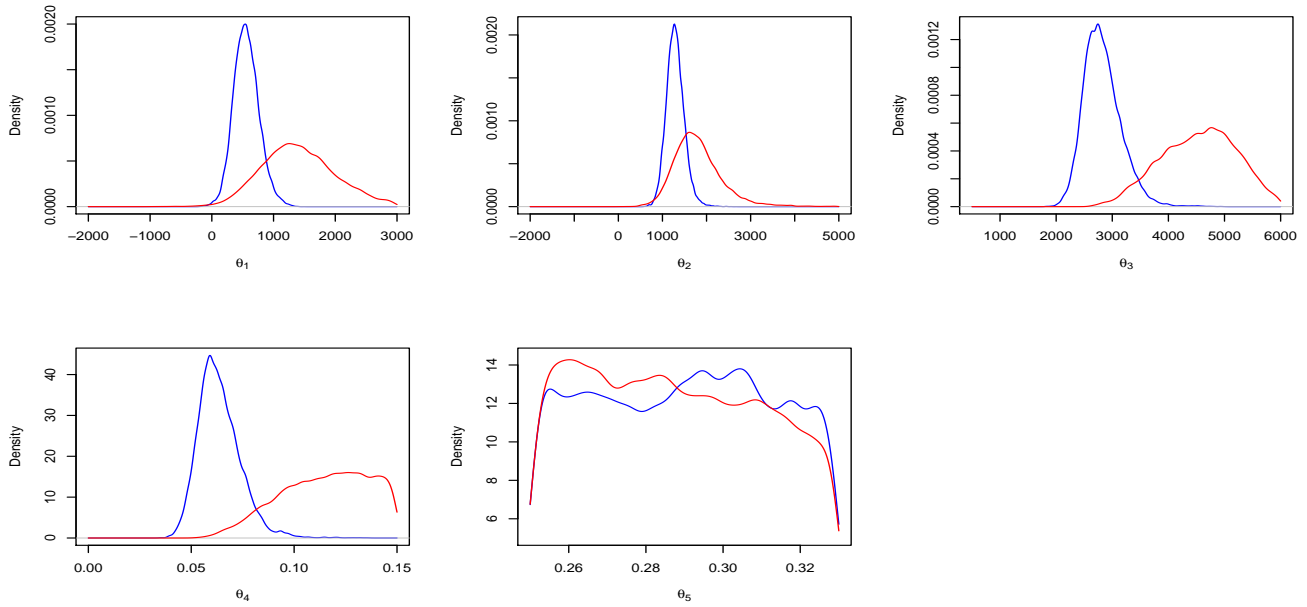


Figure 8: Marginal posterior density of θ by the GaSP (red curves) and S-GaSP (blue curve). The posterior densities of the spatial location and depth of the chamber are graphed in the first row. The posterior densities of the volume change rate of the reservoir and Poisson's ratio are graphed in the second row.

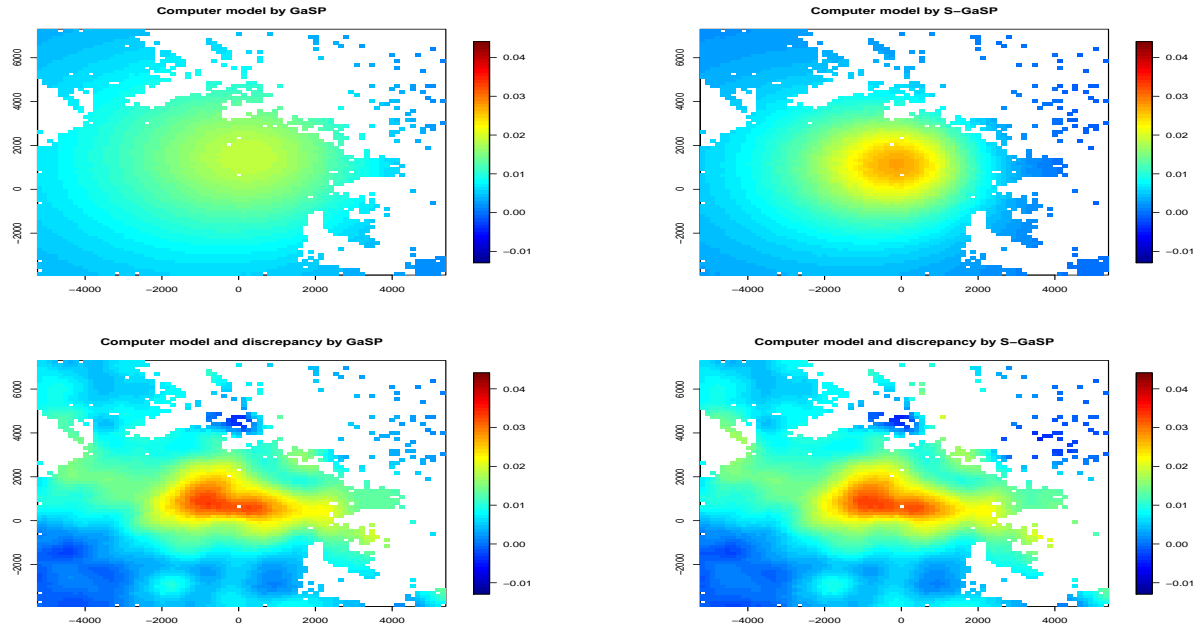


Figure 9: Prediction by different models of the first interferogram. The prediction of the calibrated geophysical model by GaSP and S-GaSP calibration is graphed in the upper left and upper right panel, respectively. The prediction of the calibrated geophysical model and discrepancy is graphed in the lower panels.

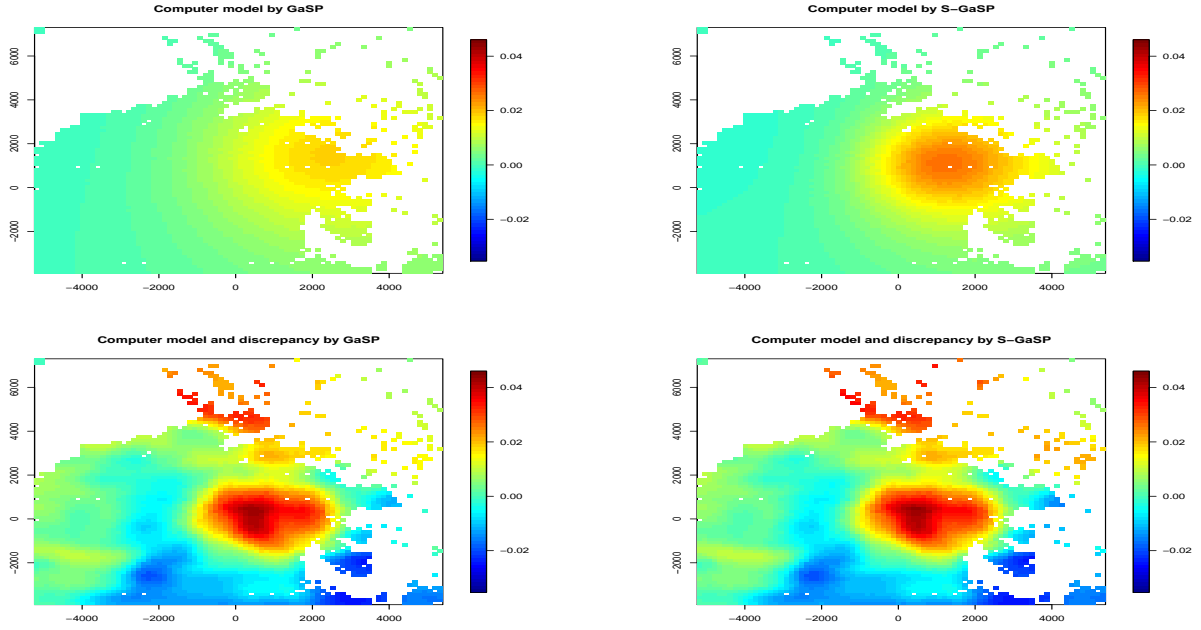


Figure 10: Prediction by different models of the second interferogram. The prediction of the calibrated geophysical model by GaSP and S-GaSP calibration is graphed in the upper left and upper right panel, respectively. The prediction of the calibrated geophysical model and discrepancy is graphed in the lower panels.

centimeters, which is larger than the one by the GaSP calibration, as a comparatively shallow chamber of the reservoir causes a larger ground displacement in a smaller area. The predictive mean squared error by the S-GaSP calibration 2.40×10^{-5} and 1.21×10^{-4} , which is smaller than the ones by the GaSP model.

Note the maximum ground deformation by the S-GaSP calibration is still a little smaller than maximum values in the hold-out images, which might be caused by the flaws in the interferograms. E.g. the ground deformation in the northern part of the second interferogram is very large, which can be caused by factors other than the volcanic activities, such as the air and ground conditions. This phenomenon is common in the InSAR data, and manually deleting these flawed pixels may be possible but costly. The S-GaSP calibration is much more robust than the GaSP calibration for these imperfect data.

As shown in the lower panels in Figure 9 and Figure 10, the prediction by the calibrated geophysical model and discrepancy by both models is much better than using the calibrated computer model alone. The predictive mean squared error by the GaSP calibration is 3.52×10^{-6} and 5.44×10^{-6} , while the predictive error by the S-GaSP calibration is 3.75×10^{-6} and 5.61×10^{-6} for the first and second interferograms, respectively. The predictive errors by both models are very small, compared to the prediction by the calibrated geophysical model alone.

5 Concluding remarks

This paper discusses the problem of calibration and prediction by integrating the computer model and field data. We analyzed the difference between the L_2 calibration and GaSP calibration, and introduced a new stochastic process called the scaled Gaussian stochastic process (S-GaSP) that bridges the gap between these two approaches. Unlike the GaSP model, the strong correlation in the data does not affect much in estimating the parameters in the computer model. We also showed the S-GaSP model can serve as a good sampling model and perform as good as the GaSP model in out of sample prediction by combining the calibrated computer model and discrepancy together. We provided a computational feasible approach of the S-GaSP model under the Bayesian framework, the computational complexity of which is the same as the GaSP model. Both simulated and real examples are provided to demonstrate the benefit of using S-GaSP in calibration.

There are a variety of open topics in the S-GaSP model for calibration. In this paper, we assume a default choice of the scaling function (mainly for the computational reason), in which the parameter λ controls the degree of shrinkage on the sample path of the S-GaSP model towards 0. We let $\lambda = n/2$ for numerical analysis in this paper, while a way to estimate λ is needed and a prior for λ may be developed to reflect the uncertainty in this parameter. It would also be interesting to discuss other choices of the scaling function. Furthermore, theoretical properties of the S-GaSP model are to be explored, such as asymptotic properties for parameter estimation and prediction.

A Proofs

proof of Lemma 1. First by Karhunen-Loève expansion, one has

$$\frac{\delta(\mathbf{x}) - \mu(\mathbf{x})}{\sigma} = \sum_{i=1}^{\infty} \sqrt{\lambda_i} Z_i \phi_i(\mathbf{x}), \quad (30)$$

where Z_i is a mean-zero unit-variance normal random variable, λ_i and ϕ_i are the i^{th} eigenvalue and normalized eigenfunction of the kernel $c(\cdot, \cdot)$ with regard to Lebesgue measure, respectively. $\{\phi_i\}_{i=1}^{\infty}$ is an orthonormal basis of the space of L_2 integrable functions defined on \mathcal{X} . As $\|\mu(\cdot)\|_{L_2(\mathcal{X})} < \infty$, one has

$$\mu(\mathbf{x}) = \sum_{i=1}^{\infty} \mu_i \phi_i(\mathbf{x}), \quad (31)$$

for some coefficients μ_i . Because

$$\begin{aligned} \langle \mu(\cdot), \phi_i(\cdot) \rangle_{L_2(\mathcal{X})} &= \left\langle \sum_{i=1}^{\infty} \mu_i \phi_i(\cdot), \phi_i(\cdot) \right\rangle_{L_2(\mathcal{X})} \\ &= \mu_i \langle \phi_i(\cdot), \phi_i(\cdot) \rangle_{L_2(\mathcal{X})} \\ &= \mu_i, \end{aligned} \quad (32)$$

where $\langle f(\cdot), g(\cdot) \rangle_{L_2(\mathcal{X})} = \int_{\mathcal{X}} f(x)g(x)dx$ for any L_2 integrable function $f(\cdot)$ and $g(\cdot)$ on \mathcal{X} . The last two equalities are due the linearity in L_2 -inner product and orthonormality of $\{\phi_i\}_{i=1}^{\infty}$, respectively.

Plugging (31) into (30), one has

$$\delta(\mathbf{x}) = \sigma \sum_{i=1}^{\infty} \left(\sqrt{\lambda_i} Z_i \phi_i(\mathbf{x}) + \frac{\mu_i \phi_i(\mathbf{x})}{\sigma} \right) = \sigma \sum_{i=1}^{\infty} \sqrt{\lambda_i} \phi_i(\mathbf{x}) \left(Z_i + \frac{\mu_i}{\sqrt{\lambda_i} \sigma} \right), \quad (33)$$

where μ_i is given in (32). The result thus follows. \square

proof of Lemma 2. Assume $f_Z(z) = f_Z(z|\Theta) = C > 0$, then (14) becomes

$$p_Z(z|\Theta) = \frac{C \cdot p_\delta \left(\int_{\xi \in \mathcal{X}} \delta(\xi)^2 d\xi = z \mid \Theta \right)}{\int_0^\infty C \cdot p_\delta \left(\int_{\xi \in \mathcal{X}} \delta(\xi)^2 d\xi = t \mid \Theta \right) dt} = p_\delta \left(\int_{\xi \in \mathcal{X}} \delta(\xi)^2 d\xi = z \mid \Theta \right). \quad (34)$$

Plugging (34) into (11), one has

$$\begin{aligned} p_{\delta_z}(\delta_z|\Theta) &= p_\delta(\delta_z|\Theta) \int_0^\infty \frac{p_\delta \left(\int_{\xi \in \mathcal{X}} \delta(\xi)^2 d\xi = z \mid \delta_z, \Theta \right)}{p_\delta \left(\int_{\xi \in \mathcal{X}} \delta(\xi)^2 d\xi = z \mid \Theta \right)} p_\delta \left(\int_{\xi \in \mathcal{X}} \delta(\xi)^2 d\xi = z \mid \Theta \right) dz \\ &= p_\delta(\delta_z|\Theta) \int_0^\infty p_\delta \left(\int_{\xi \in \mathcal{X}} \delta(\xi)^2 d\xi = z \mid \delta_z, \Theta \right) dz \\ &= p_\delta(\delta_z|\Theta), \end{aligned} \quad (35)$$

from which the results follow. \square

proof of Lemma 3. Since $\delta(\cdot) \mid \delta_z, \Theta \sim \text{GaSP}(\mu^{*\delta}(\cdot), \sigma_\delta^2 c^{*\delta}(\cdot, \cdot))$, from Lemma 1 one has

$$\int_{\mathbf{x} \in \mathcal{X}} \delta(\mathbf{x})^2 d\mathbf{x} \mid \delta_z, \Theta \sim \sigma_\delta^2 \sum_{i=1}^{\infty} \lambda_i^* \chi_{a_i^*}^2(1), \quad (36)$$

where $a_i^* = (\mu_i^*)^2 / (\lambda_i^* \sigma_\delta^2)$ with $\mu_i^* = \int_{\mathbf{x} \in \mathcal{X}} \mu^{*\delta}(\mathbf{x}) \phi_i^*(\mathbf{x}) d\mathbf{x}$. Denote $M_X(t)$ as the moment generating function for X , i.e., $M_X(t) = \mathbb{E} [e^{tX}]$. Assume X_i follows a non-central chi-square distribution with 1 degree of freedom and the non-central parameter a_i^* , then $M_{X_i}(t) = (1 - 2t)^{-1/2} e^{a_i^* t / (1 - 2t)}$ for $t < 1/2$. Moreover, let $S = \sigma_\delta^2 \sum_{i=1}^{\infty} \lambda_i^* X_i$, then

$$M_S(t) = \mathbb{E} \left[e^{\sigma_\delta^2 t \sum_{i=1}^{\infty} \lambda_i^* X_i} \right] = \prod_{i=1}^{\infty} \mathbb{E} \left[e^{\sigma_\delta^2 t \lambda_i^* X_i} \right] = \prod_{i=1}^{\infty} M_{X_i}(\sigma_\delta^2 t \lambda_i^*). \quad (37)$$

Let $\tilde{\lambda} = \lambda / (2\sigma_\delta^2 \text{Vol}(\mathcal{X}))$. Using (37), $b_1(\delta_z, \Theta)$ can be computed as follows

$$\begin{aligned} b_1(\delta_z, \Theta) &= \int_0^\infty p_\delta \left(\int_{\xi \in \mathcal{X}} \delta(\xi)^2 d\xi = z \mid \delta_z, \Theta \right) \tilde{\lambda} e^{-\tilde{\lambda} z} dz \\ &= \tilde{\lambda} M_S(-\tilde{\lambda}) \\ &= \tilde{\lambda} \prod_{i=1}^{\infty} M_{X_i}(-\sigma_\delta^2 \tilde{\lambda} \lambda_i^*) \\ &= \tilde{\lambda} \left[\prod_{i=1}^{\infty} (1 + 2\sigma_\delta^2 \tilde{\lambda} \lambda_i^*)^{-1/2} \right] e^{-\sum_{i=1}^{\infty} \frac{a_i^* \sigma_\delta^2 \tilde{\lambda} \lambda_i^*}{1 + 2\sigma_\delta^2 \tilde{\lambda} \lambda_i^*}}. \end{aligned} \quad (38)$$

For the following term in (38), one has

$$\begin{aligned}
a_i^* \sigma_\delta^2 \lambda_i^* &= \left[\int_{\mathbf{x} \in \mathcal{X}} \mu^{*\delta}(\mathbf{x}) \phi_i^*(\mathbf{x}) d\mathbf{x} \right]^T \left[\int_{\mathbf{x} \in \mathcal{X}} \mu^{*\delta}(\mathbf{x}) \phi_i^*(\mathbf{x}) d\mathbf{x} \right] \\
&= \left[\int_{\mathbf{x} \in \mathcal{X}} \mathbf{r}^\delta(\mathbf{x})^T (\mathbf{R}^\delta)^{-1} \boldsymbol{\delta}_z \phi_i^*(\mathbf{x}) d\mathbf{x} \right]^T \left[\int_{\mathbf{x} \in \mathcal{X}} \mathbf{r}^\delta(\mathbf{x})^T (\mathbf{R}^\delta)^{-1} \boldsymbol{\delta}_z \phi_i^*(\mathbf{x}) d\mathbf{x} \right] \\
&= \boldsymbol{\delta}_z^T (\mathbf{R}^\delta)^{-1} \left[\int_{\mathbf{x} \in \mathcal{X}} \mathbf{r}^\delta(\mathbf{x}) \phi_i^*(\mathbf{x}) d\mathbf{x} \right] \left[\int_{\mathbf{x} \in \mathcal{X}} \mathbf{r}^\delta(\mathbf{x}) \phi_i^*(\mathbf{x}) d\mathbf{x} \right]^T (\mathbf{R}^\delta)^{-1} \boldsymbol{\delta}_z, \tag{39}
\end{aligned}$$

where the first equality is by $a_i^* = (\mu_i^*)^2 / (\lambda_i^* \sigma_\delta^2)$ and $\mu_i^* = \int_{\mathbf{x} \in \mathcal{X}} \mu^{*\delta}(\mathbf{x}) \phi_i^*(\mathbf{x}) d\mathbf{x}$; the second equality follows from (12).

From (15), (38) and (39), one has

$$p_{\delta_z}(\boldsymbol{\delta}_z | \boldsymbol{\Theta}) \propto \exp \left\{ -\frac{1}{2} \boldsymbol{\delta}_z^T \left[\sigma_\delta^{-2} \mathbf{B} + (\sigma_\delta^2 \mathbf{R}^\delta)^{-1} \right] \boldsymbol{\delta}_z \right\} = \exp \left\{ -\frac{1}{2\sigma_\delta^2} \boldsymbol{\delta}_z^T \left[\mathbf{B} + (\mathbf{R}^\delta)^{-1} \right] \boldsymbol{\delta}_z \right\}, \tag{40}$$

where

$$\mathbf{B} = (\mathbf{R}^\delta)^{-1} \left\{ \sum_{i=1}^{\infty} \frac{\lambda}{\text{Vol}(\mathcal{X}) + \lambda_i^* \lambda} \left(\int_{\mathbf{x} \in \mathcal{X}} \mathbf{r}^\delta(\mathbf{x}) \phi_i^*(\mathbf{x}) d\mathbf{x} \right) \left(\int_{\mathbf{x} \in \mathcal{X}} \mathbf{r}^\delta(\mathbf{x}) \phi_i^*(\mathbf{x}) d\mathbf{x} \right)^T \right\} (\mathbf{R}^\delta)^{-1}, \tag{41}$$

Hence, $\boldsymbol{\delta}_z$ follows a multivariate normal distribution

$$\boldsymbol{\delta}_z | \boldsymbol{\Theta} \sim MN(\mathbf{0}, \sigma_\delta^2 \mathbf{R}_z), \tag{42}$$

with $\mathbf{R}_z = \left[\mathbf{B} + (\mathbf{R}^\delta)^{-1} \right]^{-1}$. □

proof of Lemma 4. For (22), one has

$$p_{\delta_z^a}(\boldsymbol{\delta}_z^a | \boldsymbol{\Theta}) = \frac{b_1^a(\boldsymbol{\delta}_z^a, \boldsymbol{\Theta})}{b_0^a(\boldsymbol{\Theta})} p_\delta(\boldsymbol{\delta}_z^a | \boldsymbol{\Theta}), \tag{43}$$

where

$$b_0^a(\boldsymbol{\Theta}) = \int_0^\infty p_\delta \left(\sum_{i=1}^{N_C} \delta(\mathbf{x}_i^C)^2 \Delta x = t | \boldsymbol{\Theta} \right) f_Z(t | \boldsymbol{\Theta}) dt, \tag{44}$$

$$b_1^a(\boldsymbol{\delta}_z^a, \boldsymbol{\Theta}) = \int_0^\infty p_\delta \left(\sum_{i=1}^{N_C} \delta(\mathbf{x}_i^C)^2 \Delta x = z | \boldsymbol{\delta}_z, \boldsymbol{\Theta} \right) f_Z(z | \boldsymbol{\Theta}) dz. \tag{45}$$

Apply equations (12) and (13) on $\mathbf{x}_1^C, \dots, \mathbf{x}_{N_C}^C$, we have

$$(\delta(\mathbf{x}_1^C), \dots, \delta(\mathbf{x}_{N_C}^C))^T | \boldsymbol{\delta}_z, \boldsymbol{\Theta} \sim MN(\boldsymbol{\mu}^{*C}, \sigma_\delta^2 \mathbf{R}^{*C}), \tag{46}$$

where

$$\boldsymbol{\mu}^{*C} = \mathbf{r}^C (\mathbf{R}^\delta)^{-1} \boldsymbol{\delta}_z, \tag{47}$$

and

$$\mathbf{R}^{*C} = \mathbf{R}^C - \mathbf{r}^C (\mathbf{R}^\delta)^{-1} (\mathbf{r}^C)^T. \quad (48)$$

Denote the eigen-decomposition of \mathbf{R}^{*C} as $\mathbf{R}^{*C} = \mathbf{U}^C \mathbf{\Lambda}^C (\mathbf{U}^C)^T$, where the i -th diagonal element of $\mathbf{\Lambda}^C$ is λ_i^C . From the proof of Lemma 1, one has

$$\sum_{i=1}^{N_C} \delta (\mathbf{x}_i^C)^2 \mid \boldsymbol{\delta}_z, \boldsymbol{\Theta} \sim \sigma_\delta^2 \sum_{i=1}^{N_C} \lambda_i^C \chi_{a_i^C}^2(1), \quad (49)$$

where $a_i^C = \left[(\mathbf{U}_i^C)^T \boldsymbol{\mu}^{*C} \right]^2 / (\lambda_i^C \sigma_\delta^2)$ and \mathbf{U}_i^C is the i -th column of \mathbf{U}^C . Similar to the proof in Lemma 3, defining $\tilde{\lambda}^C = \Delta x \tilde{\lambda} = \lambda / (2\sigma_\delta^2 N_C)$, we can write $b_1^a(\boldsymbol{\delta}_z^a, \boldsymbol{\Theta})$ as

$$b_1^a(\boldsymbol{\delta}_z^a, \boldsymbol{\Theta}) = \tilde{\lambda}^C M_{S^C}(-\tilde{\lambda}^C) = \frac{\lambda}{2\sigma_\delta^2 N_C} \left[\prod_{i=1}^{N_C} \left(1 + \frac{\lambda}{N_C} \lambda_i^C \right)^{-1/2} \right] e^{-\sum_{i=1}^{N_C} \frac{a_i^C \lambda \lambda_i^C}{2(N_C + \lambda \lambda_i^C)}}, \quad (50)$$

where $S^C = \sigma_\delta^2 \sum_{i=1}^{N_C} \lambda_i^C X_i^C$ for X_i^C follows a non-central chi-square distribution with 1 degree of freedom and the non-central parameter a_i^C .

Define a diagonal matrix $\mathbf{\Lambda}^{*C}$ with elements

$$[\mathbf{\Lambda}^{*C}]_{ii} = \frac{\lambda}{N_C + \lambda \lambda_i^C}, \quad (51)$$

then the following term in (50) becomes

$$-\sum_{i=1}^{N_C} \frac{a_i^C \lambda \lambda_i^C}{2(N_C + \lambda \lambda_i^C)} = -\frac{1}{2\sigma_\delta^2} (\boldsymbol{\mu}^{*C})^T \mathbf{U}^C \mathbf{\Lambda}^{*C} (\mathbf{U}^C)^T \boldsymbol{\mu}^{*C}. \quad (52)$$

Combining (43), (47), (50) and (52), it is easy to see that

$$p_{\delta_z}(\boldsymbol{\delta}_z^a \mid \boldsymbol{\Theta}) \propto \exp \left\{ -\frac{1}{2\sigma_\delta^2} \boldsymbol{\delta}_z^T \left[(\mathbf{R}^\delta)^{-1} (\mathbf{r}^C)^T \mathbf{U}^C \mathbf{\Lambda}^{*C} (\mathbf{U}^C)^T \mathbf{r}^C (\mathbf{R}^\delta)^{-1} + (\mathbf{R}^\delta)^{-1} \right] \boldsymbol{\delta}_z \right\}. \quad (53)$$

Apply Woodbury matrix identity, we have

$$\begin{aligned} & \left[(\mathbf{R}^\delta)^{-1} (\mathbf{r}^C)^T \mathbf{U}^C \mathbf{\Lambda}^{*C} (\mathbf{U}^C)^T \mathbf{r}^C (\mathbf{R}^\delta)^{-1} + (\mathbf{R}^\delta)^{-1} \right]^{-1} \\ &= \mathbf{R}^\delta - (\mathbf{r}^C)^T \mathbf{U}^C \left[(\mathbf{\Lambda}^{*C})^{-1} + (\mathbf{U}^C)^T \mathbf{r}^C (\mathbf{R}^\delta)^{-1} (\mathbf{r}^C)^T \mathbf{U}^C \right]^{-1} (\mathbf{U}^C)^T \mathbf{r}^C. \end{aligned} \quad (54)$$

Note that $(\mathbf{\Lambda}^{*C})^{-1} = N_C \mathbf{I}_{N_C} / \lambda + \mathbf{\Lambda}^C$. Hence, (54) becomes

$$\begin{aligned}
& \mathbf{R}^\delta - (\mathbf{r}^C)^T \mathbf{U}^C \left[\frac{N_C}{\lambda} \mathbf{I}_{N_C} + \mathbf{\Lambda}^C + (\mathbf{U}^C)^T \mathbf{r}^C (\mathbf{R}^\delta)^{-1} (\mathbf{r}^C)^T \mathbf{U}^C \right]^{-1} (\mathbf{U}^C)^T \mathbf{r}^C \\
&= \mathbf{R}^\delta - (\mathbf{r}^C)^T \mathbf{U}^C \left[\frac{N_C}{\lambda} \mathbf{I}_{N_C} + (\mathbf{U}^C)^T \left(\mathbf{R}^{*C} + \mathbf{r}^C (\mathbf{R}^\delta)^{-1} (\mathbf{r}^C)^T \right) \mathbf{U}^C \right]^{-1} (\mathbf{U}^C)^T \mathbf{r}^C \\
&= \mathbf{R}^\delta - (\mathbf{r}^C)^T \mathbf{U}^C \left[\frac{N_C}{\lambda} \mathbf{I}_{N_C} + (\mathbf{U}^C)^T \mathbf{R}^C \mathbf{U}^C \right]^{-1} (\mathbf{U}^C)^T \mathbf{r}^C \\
&= \mathbf{R}^\delta - (\mathbf{r}^C)^T \left[\mathbf{U}^C \left(\frac{N_C}{\lambda} \mathbf{I}_{N_C} + (\mathbf{U}^C)^T \mathbf{R}^C \mathbf{U}^C \right) (\mathbf{U}^C)^T \right]^{-1} \mathbf{r}^C \\
&= \mathbf{R}^\delta - (\mathbf{r}^C)^T \left(\frac{N_C}{\lambda} \mathbf{I}_{N_C} + \mathbf{R}^C \right)^{-1} \mathbf{r}^C \\
&= \mathbf{R}_z^a
\end{aligned} \tag{55}$$

Therefore, we conclude that

$$\delta_z^a \mid \Theta \sim MN(\mathbf{0}, \sigma_\delta^2 \mathbf{R}_z^a). \tag{56}$$

□

Acknowledgment

The authors would like to thank Kyle Anderson for providing the real example in the numerical study.

References

- Anderson, K. R. and Poland, M. P. (2016). Bayesian estimation of magma supply, storage, and eruption rates using a multiphysical volcano model: Kīlauea volcano, 2000–2012. *Earth and Planetary Science Letters*, 447:161–171.
- Anderson, K. R. and Poland, M. P. (2017). Abundant carbon in the mantle beneath hawaii/i. *Nature Geoscience*, 10(9):704–708.
- Arendt, P. D., Apley, D. W., and Chen, W. (2012a). Quantification of model uncertainty: Calibration, model discrepancy, and identifiability. *Journal of Mechanical Design*, 134(10):100908.
- Arendt, P. D., Apley, D. W., Chen, W., Lamb, D., and Gorsich, D. (2012b). Improving identifiability in model calibration using multiple responses. *Journal of Mechanical Design*, 134(10):100909.
- Bayarri, M., Berger, J., Cafeo, J., Garcia-Donato, G., Liu, F., Palomo, J., Parthasarathy, R., Paulo, R., Sacks, J., and Walsh, D. (2007a). Computer model validation with functional output. *The Annals of Statistics*, pages 1874–1906.

- Bayarri, M. J., Berger, J. O., Calder, E. S., Dalbey, K., Lunagomez, S., Patra, A. K., Pitman, E. B., Spiller, E. T., and Wolpert, R. L. (2009). Using statistical and computer models to quantify volcanic hazards. *Technometrics*, 51(4):402–413.
- Bayarri, M. J., Berger, J. O., Paulo, R., Sacks, J., Cafeo, J. A., Cavendish, J., Lin, C.-H., and Tu, J. (2007b). A framework for validation of computer models. *Technometrics*, 49(2):138–154.
- Berger, J. O., De Oliveira, V., and Sansó, B. (2001). Objective Bayesian analysis of spatially correlated data. *Journal of the American Statistical Association*, 96(456):1361–1374.
- Brynjarsdóttir, J. and O’Hagan, A. (2014). Learning about physical parameters: The importance of model discrepancy. *Inverse Problems*, 30(11):114007.
- De Oliveira, V. (2007). Objective Bayesian analysis of spatial data with measurement error. *Canadian Journal of Statistics*, 35(2):283–301.
- Forrester, A., Sobester, A., and Keane, A. (2008). *Engineering design via surrogate modelling: a practical guide*. John Wiley & Sons.
- Gu, M. (2016). *Robust uncertainty quantification and scalable computation for computer models with massive output*. PhD thesis, Duke University.
- Gu, M., Berger, J. O., et al. (2016a). Parallel partial Gaussian process emulation for computer models with massive output. *The Annals of Applied Statistics*, 10(3):1317–1347.
- Gu, M., Palomo, J., and Berger, J. (2016b). Robustgasp: Robust Gaussian stochastic process emulation. R package version 0.5.
- Gu, Mengyang, X. W. and Berger, J. O. (2017). Robust Gaussian stochastic process emulation. Technical report.
- Higdon, D. et al. (2002). Space and space-time modeling using process convolutions. *Quantitative methods for current environmental issues*, 3754.
- Higdon, D., Gattiker, J., Williams, B., and Rightley, M. (2008). Computer model calibration using high-dimensional output. *Journal of the American Statistical Association*, 103(482):570–583.
- Kennedy, M. C. and O’Hagan, A. (2001). Bayesian calibration of computer models. *Journal of the Royal Statistical Society: Series B (Statistical Methodology)*, 63(3):425–464.
- Li, R. and Sudjianto, A. (2005). Analysis of computer experiments using penalized likelihood in gaussian kriging models. *Technometrics*, 47(2).
- Liu, F., Bayarri, M., Berger, J., et al. (2009). Modularization in Bayesian analysis, with emphasis on analysis of computer models. *Bayesian Analysis*, 4(1):119–150.
- Lopes, D. (2011). *Development and implementation of Bayesian computer model emulators*. PhD thesis, Duke University.

- Massonnet, D. and Feigl, K. L. (1998). Radar interferometry and its application to changes in the earth’s surface. *Reviews of geophysics*, 36(4):441–500.
- Oakley, J. (1999). *Bayesian uncertainty analysis for complex computer codes*. PhD thesis, University of Sheffield.
- Paulo, R. (2005). Default priors for Gaussian processes. *Annals of statistics*, pages 556–582.
- Plumlee, M. (2016). Bayesian calibration of inexact computer models. *Journal of the American Statistical Association*, (just-accepted).
- Qian, P. Z. and Wu, C. J. (2008). Bayesian hierarchical modeling for integrating low-accuracy and high-accuracy experiments. *Technometrics*, 50(2):192–204.
- Ren, C., Sun, D., and He, C. (2012). Objective Bayesian analysis for a spatial model with nugget effects. *Journal of Statistical Planning and Inference*, 142(7):1933–1946.
- Roustant, O., Ginsbourger, D., and Deville, Y. (2012). Dicekriging, diceoptim: Two R packages for the analysis of computer experiments by kriging-based metamodeling and optimization.
- Sacks, J., Welch, W. J., Mitchell, T. J., and Wynn, H. P. (1989). Design and analysis of computer experiments. *Statistical science*, pages 409–423.
- Santner, T. J., Williams, B. J., and Notz, W. I. (2013). *The design and analysis of computer experiments*. Springer Science & Business Media.
- Spiller, E. T., Bayarri, M., Berger, J. O., Calder, E. S., Patra, A. K., Pitman, E. B., and Wolpert, R. L. (2014). Automating emulator construction for geophysical hazard maps. *SIAM/ASA Journal on Uncertainty Quantification*, 2(1):126–152.
- Stein, M. L. (2012). *Interpolation of spatial data: some theory for kriging*. Springer Science & Business Media.
- Tuo, R. and Wu, C. J. (2016). A theoretical framework for calibration in computer models: parametrization, estimation and convergence properties. *SIAM/ASA Journal on Uncertainty Quantification*, 4(1):767–795.
- Tuo, R., Wu, C. J., et al. (2015). Efficient calibration for imperfect computer models. *The Annals of Statistics*, 43(6):2331–2352.
- Wong, R. K., Storlie, C. B., and Lee, T. (2017). A frequentist approach to computer model calibration. *Journal of the Royal Statistical Society: Series B (Statistical Methodology)*, 79(2):635–648.